



HHS Public Access

Author manuscript

IEEE Trans Mol Biol Multiscale Commun. Author manuscript; available in PMC 2023 June 30.

Published in final edited form as:

IEEE Trans Mol Biol Multiscale Commun. 2023 March ; 9(1): 28–48. doi:10.1109/tmbmc.2023.3246928.

Drug Cocktail Formulation via Circuit Design

Douglas Raymond Beahm,

Thayer School of Engineering, Dartmouth College, Hanover, NH 03755 USA

Yijie Deng,

Thayer School of Engineering, Dartmouth College, Hanover, NH 03755 USA

Thomas M. DeAngelo,

Thayer School of Engineering, Dartmouth College, Hanover, NH 03755 USA

Rahul Sarpeshkar [Fellow, IEEE]

Departments of Engineering, Physics, Microbiology & Immunobiology, and Molecular & Systems Biology, Dartmouth College, Hanover, NH 03755 USA

Abstract

Electronic circuits intuitively visualize and quantitatively simulate biological systems with nonlinear differential equations that exhibit complicated dynamics. Drug cocktail therapies are a powerful tool against diseases that exhibit such dynamics. We show that just six key states, which are represented in a feedback circuit, enable drug-cocktail formulation: 1) healthy cell number; 2) infected cell number; 3) extracellular pathogen number; 4) intracellular pathogenic molecule number; 5) innate immune system strength; and 6) adaptive immune system strength. To enable drug cocktail formulation, the model represents the effects of the drugs in the circuit. For example, a nonlinear feedback circuit model fits measured clinical data, represents cytokine storm and adaptive autoimmune behavior, and accounts for age, sex, and variant effects for SARS-CoV-2 with few free parameters. The latter circuit model provided three quantitative insights on the optimal timing and dosage of drug components in a cocktail: 1) antipathogenic drugs should be given early in the infection, but immunosuppressant timing involves a tradeoff between controlling pathogen load and mitigating inflammation; 2) both within and across-class combinations of drugs have synergistic effects; 3) if they are administered sufficiently early in the infection, antipathogenic drugs are more effective at mitigating autoimmune behavior than immunosuppressant drugs.

Index Terms—

Analog circuits; biological circuits; circuit techniques for drug design; COVID-19; drug cocktail evaluation; SARS-CoV-2

This work is licensed under a Creative Commons Attribution-NonCommercial-NoDerivatives 4.0 License. For more information, see <https://creativecommons.org/licenses/by-nc-nd/4.0/>

Corresponding author: Rahul Sarpeshkar. rahul.sarpeshkar@dartmouth.edu.

This article has supplementary downloadable material available at <https://doi.org/10.1109/TMBMC.2023.3246928>, provided by the authors.

I. Introduction

DYNAMIC models of host-pathogen interactions fitted to clinical data can bring critical insights to the complexity of multiple diseases and provide valuable information for the development of treatments. For example, a dynamic circuit model can serve as a foundational tool for rapid drug cocktail formulation in the current pandemic, future pandemics, or other diseases, even in non-viral pathogens and cancers. Circuit models explicitly visualize underlying relationships among components in biological systems while simultaneously being an exact mathematical representation of the underlying equations [1], [2], [3], [4], [5], [6]. Building from this established theoretical foundation, circuit models have achieved a strong track record of fitting data from synthetic and naturally occurring biological systems [6], [7], [8], [9] but have not thus far been applied towards principled approaches to drug-cocktail formulation.

Clinically, combining drugs into cocktails to achieve synergistic effects has been a key strategy in combating viral diseases. For decades, combination antiretroviral therapy has been the standard of care for the management of HIV [10]. More recently, anti-HIV broadly neutralizing antibodies (bNAbs) are also being studied in cocktail formulations [11], with exploration towards combining antiretroviral cocktails and bNAb cocktails into multi-class cocktails [12]. In the context of influenza, several novel drugs that target viral and host factors have reached clinical trials as synergistic combination therapies with oseltamivir, an established monotherapy, with both positive and negative results [13], [14], [15]. Inspired by these prior clinical antiviral combination therapies, we aimed to innovate *in silico* drug-cocktail formulation and discovery via a circuit design approach. Although our methods can be applied to several diseases, in this paper, we shall focus on COVID-19.

The COVID-19 pandemic, caused by the SARS-CoV-2 coronavirus and its ensuing variants, has disrupted society and the economy around the world. As of February 1, 2023, the World Health Organization had reported totals of 754 million cases and 13.2 million deaths worldwide [16]. Boosted vaccination against SARS-CoV-2 significantly reduces the rates of symptomatic infection, morbidity, and mortality, but varied host response strengths and waning protection efficacies are frequently reported among the vaccinated population [17], [18], [19], [20], [21]. For example, fully vaccinated and boosted individuals can still suffer severe disease due to breakthrough infections [22], [23]. Similar to vaccination, host responses to SARS-CoV-2 infection differ greatly and the currently available drugs against COVID-19 have shown varying efficacy among patients [24], [25], [26], [27], [28], [29], [30], [31], [32], [33], [34], [35], [36], [37]. Therefore, it is useful to study and analyze virus-host interactions and drug treatment courses for COVID-19 quantitatively.

There exist many models of within-host SARS-CoV-2 infection. The simplest variety of model does not account for the host immune response beyond first-order viral clearance and infected cell death rate constants [38], [39], [40], [41]. Another approach is to model the adaptive immune response exclusively, with no infection dynamics [42]. However, SARS-CoV-2 infection calls for models that incorporate virus-host cell infection dynamics together with the immune response [43]. Such a synergy is especially important for COVID-19, wherein strong immunity will prevent and clear infection, but overactive immunity can

lead to cytokine storm or autoimmunity. Several groups have used mathematical methods to combine models of infection kinetics and immune response dynamics [39], [40], [44], [45], [46], [47], [48], [49], [50], [51]. Some of these papers also include monotherapy and combination therapy effects; cytokine storm; age and sex effects; vaccination effects; and separate adaptive and innate immune responses, but no model in the literature has all of these features and no model includes adaptive autoimmunity or accounts for viral variant effects. An alternative modeling strategy is to apply well-studied engineering principles and tools to the COVID-19 modeling problem, as has been done with the application of chemical engineering simulation software for batch reaction kinetics to the modeling of the epidemiological dynamics of SARS-CoV-2 [52].

In our study, we employed an electronic circuit modeling approach to construct a within-host model of COVID-19 with interactions between the virus, host, and drugs. We first developed a simplified dynamic model of host-virus-drug interactions that fit clinical data across mild and severe COVID-19, while also establishing regimes of cytokine storm and adaptive autoimmune behaviors. Then, we accounted for the effects of patient age and sex and viral variant on COVID-19 dynamics. Having established the model, we used it to evaluate the timing and combination of five drug treatments for COVID-19: an anti-S monoclonal antibody (anti-S mAb), Molnupiravir (Mol), Paxlovid (Pax), Dexamethasone (Dex), and Tocilizumab (Toc).

II. Circuit Model Rationale and Development

Prior work has developed mechanistically detailed models of COVID-19 viral replication with specific viral protein and molecule species [53] and host lung and immune system responses with several specific cellular subprocesses [49] and signaling pathways [50]. However, especially with a novel disease, creating realistic dynamic behavior using many cellular, molecular, and protein species-specific parameters can be prohibitive. Additionally, the human immune system is highly complex with many intra- and inter-cellular signaling and effector systems across several cell types; thus, no human immune system model that is complete and fits quantitative experimental data yet exists [54], [55], [56], [57]. Therefore, to model COVID-19, including virus-host interactions and combinatorial drug effects, we developed a biological circuit model with six main states: healthy lung epithelial cell number (HC); infected lung epithelial cell number (IC); extracellular viral population virion number (Vpop); intracellular viral protein and molecule number (VPM); the strength of the innate immune response (II); and the strength of the adaptive immune response (AI).

The dominant interactions between the six main states, and the modulation of those interactions by drugs, are described by Fig. 1. (1) Healthy cells (HC) modulate their net growth rate to attempt to maintain a homeostatic population size. (2) At the time of infection, an initial amount of virus infects the healthy cells, creating infected cells (IC). (3) The replicating virus hijacks infected cells to produce viral proteins and molecules (VPM). (4) If the infected cell produces large numbers of viral proteins and molecules, the cell's material and energetic resources can be overwhelmed and the cell will die. (5) Infected cells release fully formed virions, causing infection to progress, but these virions can be bound and neutralized by the anti-S mAb. The production of (3) intracellular viral species (VPM)

and (5) fully formed virions (Vpop) are inhibited by Mol and Pax. (6) As they become larger in quantity, the three viral states – IC, Vpop, and VPM – trigger the innate immune response (II) (e.g., via pattern recognition receptors and cytokine release). (7) Together with that innate immune response, the three viral states are then able to trigger the adaptive immune response (AI) (e.g., via MHC antigen presentation).

The (8, 9) innate and (10, 11) adaptive immune responses are sustained by local positive feedback loops that are uncontrolled (8, 10) or controlled by the level of infection (9, 11). Strong activation of the uncontrolled innate immunity local positive feedback loop (8) can cause a cytokine storm. Other interaction-example pairings are: (9) innate immunity's controlled positive feedback and chemokine signaling; (10) adaptive immunity's uncontrolled positive feedback and the accumulation of antibodies produced by plasmablasts and plasma B cells; and (11) adaptive immunity's controlled positive feedback and B-cell affinity maturation. (12) In the presence of ongoing infection, the adaptive immune response can further grow the innate immune response (e.g., via cytotoxic T-cell cytokine production). Dex limits all productive sources of both immune responses, while Toc only reduces the value of the innate immune state, which correlates with inflammation. As a non-specific inflammatory immune response, the innate immune response kills both (13) healthy cells and (14) infected cells (e.g., via TNF α production [58]). (15) In contrast, the adaptive immune response only significantly targets infected cells for killing (e.g., via cytotoxic T-cells). Both the (16, 17) innate and (18, 19) adaptive immune responses remove virions (16, 18) (e.g., via phagocytosis and antibody-mediated opsonization, respectively), but the immune cells are susceptible to viral infection (17, 19).

For simplicity, a few features and states are not shown in Fig. 1, but are represented by our circuit models (and associated mathematics): 1) Vpop, VPM, II, and AI all have intrinsic half-life decays; 2) as VPM approaches zero after infection, infected cells recover to healthy cells (i.e., a cell is not infected if it no longer contains viral proteins or molecules); 3) there is an immunological memory state (e.g., memory B-cells) that, when non-zero, increases the sensitivity and speed of the adaptive immune response; 4) there is an adaptive autoimmunity (AAI) state that parallels the AI state; 5) Triggering AAI requires stronger infection and inflammation than AI, but AAI targets the innate immune response and healthy cells [59], [60].

In order to reduce the number of parameters needed to populate the circuit, the model states were normalized to be in the range [0, 1], i.e., from the basal level to the maximal level (or, for HC from no healthy cells to the homeostatic population size). Such normalization gave us the flexibility to capture disease dynamics with a wide dynamic range at different orders of magnitude and allowed us to make the reasonable assumption that most saturation constants are approximately 0.5 normalized units (n.u.), half of the maximum state value [61], [62]. Another model design decision was to consider the model's states as relative changes from their basal, uninfected values. For example, there are basal levels of cytokines or phagocytic cells in the innate immune system when no viral infection is present, but we initialize the II state as $II_0 = 0$. In the context of model rates, we assumed that basal rates of cell death and population growth are negligible compared to those caused by infection and recovery. For example, we do not include an intrinsic death rate of infected cells because

it would be insignificant compared to the infected cell death caused by infection and the subsequent immune response.

III. Circuit Design

It is useful to visualize our biological circuit models as electronic circuits, which represent the state variables (molecular concentrations or cell population numbers) as voltages and the flow variables (the derivative or rate-of-change variables) as currents. The circuit representation allows for intuitive identification of connections between states and the resulting feedback loops without having to parse long lists of differential equations [2], [3], [5], [6]. At the same time, the circuit representation is more quantitative than a flow diagram because each component represents a term in a mathematical equation. We designed and simulated all circuits in industry-standard Cadence Virtuoso integrated circuit design software (see Method S-C in the Supplementary Methods, Tables, and Figures and find all Cadence files in the Supplementary Code).

For several frequently used components, Fig. 2 gives the conversion from electronic circuit component to mathematical equation. These components are wired together to construct biological circuits. The COVID-19 biological circuit for viral replication is shown in Fig. 3 (a) and the biological circuits for the innate and adaptive immune responses are presented in Figs. 3 (b) and (c), respectively. The biological circuit for adaptive autoimmunity (not shown) is identical to the adaptive immunity circuit in Fig. 3 (c) but with updated names (i.e., ‘AI’ becomes ‘AAI’) for the states and some parameters. A more traditional – but mathematically equivalent – differential equation representation of the circuit model is provided in Table I, with the parameters and their values described in Table S-I in the Supplementary Methods, Tables, and Figures. A third way to represent the system is via a feedback diagram, which can be constructed by observing the state interactions described by the model’s biological schematic (Fig. 1), circuit schematic (Fig. 3), or differential equations (Table I). An example feedback diagram highlighting the interactions between viral infection, the innate immune response strength, and the adaptive immune response strength is given in Fig. S-1 in the Supplementary Methods, Tables, and Figures.

IV. Model Parameterization and Data Fitting

For the COVID-19 circuit model to be legitimate, it needed to have parameters that both agreed with literature and produced dynamics that fit clinical data. The most consequential parameters for creating the model’s global behavior were the rate constants, the values of which are given in Table S-I.a. The calculation of these rate constants from literature and their subsequent fitting to clinical data (resulting in the curves shown in Fig. 4), are described in Method S-A. Non-rate model parameters are given in Table S-I.b. The fitted clinical data is available in the Supplementary Data.

The dynamics of the model’s six main states for the mild and severe diseases follows a general pattern (Figs. 4 (a) and (d)). When an initial amount of extracellular virus (V_{pop}) infects cells and replicates to infect more cells, the number of healthy lung epithelial cells (HC) decreases while the number of infected lung epithelial cells (IC) increases. At the

same time, the number of extracellular virions (Vpop) and the number of intracellular viral proteins and molecules (VPM) increases. Eventually, viral antigens (from IC, Vpop, and VPM) accumulate to a level that activates the immune system. The innate immune response (II) is easier to trigger but is transient. The adaptive immune response (AI) is persistent but requires both antigen and innate immunity stimulation to become activated. Realistically, the adaptive immune response would eventually wane over time due to the T_{reg} calming of the T-cell response and the shift of antibody production from short-lived plasmablasts to long-lived plasma B cells in the bone marrow [65], [66]. However, these effects are beyond the scope of our model for acute COVID-19.

The dynamic differences over the infection course between the mild and severe diseases were significant, as shown in the model's fit to severity-categorized clinical data (Figs. 4 (b), (c), (e), (f)). As clinically observed, our model showed that severe disease patients generally have a larger viral load and fewer healthy cells than patients with mild disease do. Such differences were explained by changes in only two sets of parameters in our model, namely the activation K_d constants for triggering the innate and adaptive immune responses (processes 6 and 7, respectively, in Fig. 1). The activation K_d parameter differences are given in Table S-I.c. In the model of severe disease, the innate and adaptive immune systems required a higher level of infection (IC, Vpop, VPM) to trigger an immune response. In other words, severe patients in the model experienced less sensitive innate and adaptive immune detection of SARS-CoV-2 infection, corresponding to higher immune activation K_d values; poorer antigen detection allowed the disease to progress and worsen in severity before an immune response was mounted. For the selection and normalization of the clinical data, see Method S-B. Using model parameters relevant in literature and severity-specific immune activation K_d values, our circuit model captured dynamic clinical data faithfully.

Additionally, the model recapitulated common COVID-19 complications, specifically cytokine storm and adaptive autoimmunity. Model parameters were selected to make the host susceptible or resistant to either complication. For cytokine storm, a susceptible host had a lower activation K_d for the innate immune response's uncontrolled positive feedback loop (process 8 in Fig. 1) compared to the resistant host (default). For adaptive autoimmunity, a susceptible host had lower activation K_d values for more easily triggering an adaptive autoimmune response (the AAI process analogous to the AI process 7 in Fig. 1) compared to the resistant host (default). The complication-resistant and complication-susceptible parameters are given in Table S-I.d. Fig. S-2 illustrates what the cytokine storm and adaptive autoimmunity susceptible model simulations look like for severe disease. The complication-resistant parameters were used in later simulations unless explicitly stated otherwise.

Finally, the model's adaptive immunity memory (AImem) state was used to model COVID-19 in individuals who have been vaccinated or previously infected. In the model, having an immunological memory of COVID-19 effectively reduced the adaptive immunity activation K_d and increased the activation rate for the adaptive immune response (process 7 in Fig. 1). For individuals with prior infection or vaccination, the adaptive immunity memory state was initialized to $AImem_0 = 1$ n.u. (Table S-I.e). In contrast, $AImem_0 = 0$ n.u. was used for individuals who are SARS-CoV-2 naïve and unvaccinated (Table S-I.e).

A comparison between simulations with and without prior infection or vaccination is given in Fig. S-3, with the infection dynamics being less severe for the former, as expected. If the vaccination or prior infection had occurred within the previous several months, then its disease-mitigating effects may be even stronger since the initial level of antibodies would be non-zero, meaning AI_0 would be non-zero in the model [67], [68]. To be conservative and assume the worst-case scenario, all other simulations in this work assumed an unvaccinated host with no prior infection.

V. Modeling the Effects of Age, Sex, and Viral Variant

COVID-19 has shown differential effects on individuals based on their age and sex, with people of older age and male sex having worse outcomes [69], [70], [71]. To make our model more robust to these differences, we included age and sex-specific multiplicative parameters in our model. For both age and sex, multiplicative factors scaled the efficacy of the innate immune response (processes 14 and 16 in Fig. 1) and both the activation sensitivity (process 7 in Fig. 1) and positive feedback strength (processes 10 and 11 in Fig. 1) of the adaptive immune response. The placement of these multiplicative factors within the model's ODEs is described in Table S-II.a. The multiplicative parameters' values are described in Table S-II.b. For context, the young age parameters represent an individual approximately in their 30s and the old age parameters represent an individual approximately in their 60s [72], [73], [74], [75].

Assuming severe disease, the combinatorial effects of age and sex on the COVID-19 model dynamics are shown in Fig. 5. Consistent with epidemiological observations, the young female simulation had the most favorable disease course while the old male simulation had the least favorable (Figs. 5 (a)–(d)). Most noticeably, the larger innate immune response from the old male simulation was indicative of excessive inflammation (Fig. 5 (e)). In the adaptive immune response, there was a cross-over in the dynamics (Fig. 5 (f)) between the different ages and sexes. This cross-over occurred because the old/male person's less effective innate immune response left more antigen to activate a strong adaptive immune response early in the infection, but the strength of the young/female person's adaptive immunity positive feedback allowed for the young/female person's adaptive immune response to surpass the old/male person's response over time. Overall, the model suggested that age has a stronger effect on disease dynamics than sex because age dominated whether the disease dynamics were more or less favorable compared to default settings (when all age and sex multipliers are set to 1).

Another determinant of COVID-19 infection parameters [76], [77], and probably outcomes [78], [79], [80], [81], [82], is the SARS-CoV-2 variant type. To account for variant-to-variant differences, we included multiplicative parameters that scale the virus' infection rate of healthy cells (process 2 in Fig. 1) and evasion of the adaptive immune response (processes 15 and 18 in Fig. 1). The placement of these multiplicative factors within the model's ODEs is described in Table S-II.a. The multiplicative parameters' values are described in Table S-II.b. The model would be more accurate with an innate immunity evasion parameter rather than an adaptive immunity evasion parameter because this would make the immune evasion strength independent of the modeled person's prior infections and vaccinations. However,

though strong studies have been performed on innate immunity evasion in individual variants [83], quantitative measurements across variants are not available.

Assuming severe disease in an old male, the effects of variants D614G (default), Alpha, Beta, and Delta on COVID-19 infection dynamics are displayed in Fig. 6. Compared to D614G, the Alpha variant had dynamics that were similar in magnitude, but faster. These differences are attributable to Alpha's higher cellular infection rate but poorer adaptive immunity evasion (Table S-II.b). The Beta and Delta variants caused simulation dynamics that are equally large in magnitude but opposing in strategy. The Beta variant's powerful evasion of adaptive immunity allowed it to achieve the highest peak viral load of all the variants (Fig. 6 (c)). In contrast, the Delta variant's extremely high rate of cellular infection enabled it to peak fastest in its effects on epithelial cell populations (Figs. 6 (a) and (b)) and viral states (Figs. 6 (c) and (d)) without triggering a larger immune response than the Beta variant (Figs. 6 (e) and (f)). Based on our simulation results, it is reasonable to propose that the Delta variant's faster infection dynamics were a key determining factor in the Delta variant becoming the dominant variant in the human population over the D614G, Alpha, and Beta variants. We would expect that the Omicron variant has even faster infection dynamics than the Delta variant.

For both the Beta and Delta variant in Fig. 6, the infection is very serious. The number of healthy lung epithelial cells drops to a fifth of the homeostatic value (Fig. 6 (a)) and the magnitudes of the innate and adaptive immune responses are at least double the immune response magnitudes resulting from the D614G and Alpha variants (Figs. 6 (e) and (f)), increasing the risk for cytokine storm and adaptive autoimmunity complications. As a result, therapeutic drugs and drug cocktails must be examined to make the infection dynamics less severe.

VI. Rationale and Development of Drug Pharmacokinetics and Pharmacodynamics Models

Based on the platform of our virus-host interaction model validated above, we sought to model the pharmacokinetics and pharmacodynamics of potential drug interventions. The effects of five drugs on COVID-19 dynamics were examined in the model: an anti-S monoclonal antibody (anti-S mAb), Molnupiravir (Mol), Paxlovid (Pax), Dexamethasone (Dex), and Tocilizumab (Toc). The anti-S mAb dosing and kinetics are based on the REGEN-COV casirivimab/imdevimab cocktail, but a specific mAb or mAb cocktail can be substituted in response to whichever mAb or mAb cocktail is effective against the suspected or dominant variant at the time of infection. To classify the drugs, we will refer to anti-S mAbs, Mol, and Pax as "antivirals" and Dex and Toc as "immunosuppressants."

The drugs' pharmacokinetic models were chosen to have a pulse administration and first-order decay, which in electronics is equivalent to a parallel I-R-C circuit (Fig. S-4). Treatment start times, dose timing, and dose amount were informed by NIH treatment guidelines and clinical trial procedures (Tables S-III.a and S-III.b). The drugs' half-lives and their electrical-equivalent first-order RC time constants are listed in Table S-III.c. A comparison between the pharmacokinetics of the anti-S mAb (a single dose with

slow decay) and Pax (frequent doses with fast decay) demonstrated the range of the pharmacokinetic model's behaviors (Fig. S-5).

Based on each of the five drugs' mechanisms of action, we incorporated the drugs' pharmacodynamics into the COVID-19 circuit model, as presented in Figs. 1 and 3 and Table I. The anti-S mAb binds extracellular virions (V_{pop}) and prevents them from infecting cells. As a nucleoside analogue and a protease inhibitor, respectively, Mol and Pax inhibit the production of extracellular virions (V_{pop}) and intracellular viral proteins and molecules (VPM). As a glucocorticoid, Dex has systemic effects [84], [85] and therefore it was modeled as broadly inhibiting the activation and positive feedback of the immune response (II, AI, and adaptive autoimmunity). Toc is an anti-IL-6 receptor mAb and therefore it was modeled as blocking the inflammatory aspects of the innate immune response (II). The saturation constant (K_d) for each drug was taken or estimated from literature and is listed in Table S-IV.

The design choice to construct a simplified 6-state model caused a tradeoff with pharmacodynamic modeling granularity; the 6-state model may not capture some drugs' specific mechanism of action (e.g., exact biochemical targets), but the it is much faster to implement and parametrize. For example, as discussed above, Mol and Pax both inhibit the production of V_{pop} and VPM by different mechanisms: the former is a nucleoside analogue and the latter is a protease inhibitor. However, in our model, their actions were modeled in a mechanistically identical way.

VII. Single-Drug Treatment Simulations

Before formulating a drug cocktail, it was essential to understand each drug's effect on the system as a monotherapy. To best challenge the drugs, we simulated the drugs' performance under worst-case scenario conditions, namely severe disease, old age, male sex, and Delta variant. To determine the suggested time to start the monotherapy treatment courses, we reviewed NIH treatment guidelines and clinical trial procedures (see Table S-III.a). For severe disease, these treatment start times, which we refer to as the "guidance" timings, were 6 to 8 days post-infection (dpi) for anti-S mAb, Mol, and Pax; 10 dpi for Dex; and 12.5 dpi for Toc.

When following the late guidance timing of 8 dpi (i.e., 5 days post-symptom onset for severe disease), the anti-S mAb only moderately improved the disease dynamics compared to no drugs (Figs. 7 (a) and (b)). Free virions (V_{pop}) were quickly bound by the anti-S mAb, causing the other viral states (IC, VPM) to decline, but the healthy cell population (HC) had already been more than halved by the time of anti-S mAb administration and inflammation from the innate immune response (II) was mostly unchanged (Fig. 7 (b)). In contrast, the 6 dpi early guidance timing (i.e., 3 days post-symptom onset for severe disease) for the anti-S mAb essentially halted disease progression before it could become serious (Fig. 7 (c)). Before the anti-S mAb could be administered, the healthy cell population only declined by less than 20% (Fig. 7 (c)). Then, when the anti-S mAb bound the free extracellular virions, no more healthy cells could be infected while the existing infected cells either died from

their infection, were cleared by the moderate innate immune response, or recovered after their intracellular viral proteins and molecules degraded (Fig. 7 (c)).

Similarly, for Pax, the late drug guidance timing (5 days post-symptom onset – i.e., 8 dpi in severe disease) was not optimal (Fig. 8). While the 8 dpi Pax did reduce the peak viral load (Fig. 8 (b)), the number of infected cells remained high (Fig. 8 (a)) and the inflammatory peak of the innate immune response was only slightly reduced (Fig. 8 (c)). In contrast, the minimum drug guidance timing, with Pax administered 3 days post-symptom onset (i.e., 6 dpi in severe disease), was much more effective (Fig. 8). When administered at 6 dpi, Pax lowered the viral load, number of infected cells, and innate immunity inflammation to levels similar to those seen in the anti-S mAb simulation (Figs. 7 (b) and 8). The dynamics of all six main model states from the Pax simulations are shown in Fig. S-6. The simulation results for Mol were nearly identical to those for Pax and are available in Fig. S-7. In summary, starting antiviral drugs (anti-S mAb, Mol, or Pax) as early as guidance allows was essential for the antivirals' efficacy.

For the immunosuppressants, Dex and Toc, setting the treatment start time was a trade-off between the management of inflammation and viral load (Fig. 9). Our model predicted that if immunosuppressants were given following the drug timing guidance (10 dpi for Dex and 12.5 dpi for Toc), it would be too late for the immunosuppressants to be beneficial because the inflammation had already peaked (Figs. 9 (b) and (e) – red curves). In the case of Dex, the primary effect of 10 dpi administration was a weakening of the adaptive immune response, the decline of which is not desirable (Fig. 9 (c) – red curve). In contrast, if the immunosuppressants were administered at a slightly earlier time, they successfully reduced the magnitude (Dex) or duration (Toc) of the peak levels of inflammation, reducing the risk of cytokine storm or adaptive autoimmunity (Figs. 9 (b) and (e) – green curves). However, if the immunosuppressants were given too early during the disease, the viral load became very large (Toc) or uncontrollable (Dex) because the immune response was too weak to limit the infection (Figs. 9 (a) and (d) – blue curves). More specifically, when the Dex was given too early (8 dpi), the innate and adaptive immune responses were never strong enough (until after Dex treatment was over) to remove extracellular virions faster than they could be produced. In comparison, when Toc was given too early (7.5 dpi), the viral load eventually came under control during the Toc treatment (Fig. 9 (d) - blue curve) because Toc weakened only the innate immune response and not the adaptive immune response (Figs. 9 (e) and (f) – blue curves). The dynamics of all 6 main model states for the simulations shown in Fig. 9 are given in Figs. S-8 and S-9 for Dex and Toc, respectively. In summary, to find the optimum start time for immunosuppressive treatments, multiple simulations with different treatment start times should be performed and compared.

VIII. DRUG COCKTAIL FORMULATION SIMULATIONS

Using the original drug parameters from literature (Tables S-III.b, S-III.c, and S-IV), the five drugs appeared efficacious when modeled as monotherapies. However, the parameters underlying that success should be approached conservatively, especially the bioavailability and reported saturation constants (K_d) of the drugs. The bioavailability of a drug at the site of action may be lower than measured or assumed, which would cause the modeled

drug concentration to be an overestimate. Also, a drug's effective saturation constant (K_d) may be higher *in vivo* than values reported from *in vitro* experiments. Therefore, prior to beginning drug cocktail formulation, we assumed that the drugs' efficacy *in vivo* would be generally poorer than predicted. Thus, we increased the drugs' saturation constants to model the drugs' clinical performance being generally weaker. This decision served two purposes. One, it makes the simulations of drug effects more conservative and, thereby, possibly more accurate. Two, it allows us to easily explore the synergistic effects of drug cocktail designs, which we wouldn't see as clearly if monotherapies were already sufficient for clearing infection or reducing inflammation. To select the sub-optimal K_d values used to weaken the drugs' effects, we simulated several candidate order-of-magnitude changes in K_d for each drug and chose the order-of-magnitude change that gave the most intermediate response during simulated monotherapy treatment (Fig. S-10). The selected sub-optimal, or "high," K_d values were $10^4 * K_{d,mAb}$, $10^3 * K_{d,Mol}$, $10^3 * K_{d,Pax}$, $10^2 * K_{d,Dex}$, and $5 * 10^2 * K_{d,Toc}$. The values were used in all subsequent simulations unless noted otherwise.

The first cocktail that we investigated used the 3 antiviral drugs (anti-S mAb, Pax, and Mol) at their optimized 6 dpi timing. As shown in Fig. 10, each additional drug added to the cocktail synergistically improved the cocktail's efficacy. Viral load, infected cells, and inflammation all decreased while the number of healthy cells increased. The only, minor, downside was that a treated infection produced less antigen to stimulate adaptive immunity, meaning that the adaptive immune response became weaker as the antiviral cocktail improved (Fig. 10 (f)). In reality, this weaker adaptive immune response could be easily compensated for by vaccinating the host after the infection has cleared [86], [87].

The second cocktail that we simulated used the 2 immunosuppressant drugs, Dex and Toc, administered at 9 dpi and 10 dpi, respectively. These drugs worked together synergistically, reducing the peak (Dex) and period (Toc) of innate immunity inflammation (Fig. 11 (a)). The immunosuppressant cocktail only reduced the peak value of I_f by 14%, but the time the I_f state was above 0.2 n.u. (approximately 50% of the maximum value) fell by 50%. Therefore, due to the shorter duration and weaker strength of innate immune response positive feedback, there was a lower risk for triggering cytokine storm or adaptive autoimmunity. Whereas the antiviral drug cocktail curtailed the innate immune response by reducing the amount of viral antigen, the immunosuppressant cocktail reduced the innate immune response by blocking inflammatory cytokine signaling via Toc and transiently weakening the immune system's positive feedback loop-gains via Dex (Figs. 11 (a) and (b)). Again, the weaker adaptive immune response that results from this immunosuppressive cocktail can be compensated for by vaccinating the individual after the disease course [86], [87]. The full dynamics of all states for the immunosuppressant cocktail are given in Fig. S-11.

In Fig. 12, we combined the antiviral and immunosuppressant cocktails into a single, multifunctional cocktail. The antiviral drug timings were maintained from prior optimization (6 dpi for anti-S mAb, Mol, and Pax). To control the viral load, the immunosuppressant cocktail treatment start times were delayed to 10 dpi and 13 dpi for Dex and Toc, respectively. The model predicted that the use of the antiviral drug cocktail early in the disease course suppresses viral load such that it was largely unnecessary to administer

immunosuppressant drugs later in the disease course (Fig. 12 (a)). Nevertheless, Dex and Toc still served to decrease the peak and period of innate immunity inflammation (Fig. 12 (b)), reducing the risk of triggering a cytokine storm or adaptive autoimmunity. The cost of using the immunosuppressants was that the adaptive immune response also weakened (Fig. 12 (c)), which, combined with the suppressed innate immune response, allowed for a longer tail of viral infection (Fig. 12 (a)). The full dynamics of all states for the multifunctional cocktail are given in Fig. S-12.

IX. Cocktails Against Cytokine Storm and Autoimmunity

Finally, we tested whether either the antiviral or immunosuppressant drug cocktails could avert cytokine storm and adaptive autoimmunity complications (Fig. 13). For these simulations, we used the cytokine storm and adaptive autoimmunity complication-susceptible parameters described previously (Table S-I.d and Fig. S-2). The antiviral cocktail, despite using the sub-optimal K_d parameters, completely avoided the cytokine storm (Fig. 13 (c)) and minimized autoimmunity until after the viral load had subsided (Fig. 13 (b) and (d)). As a result, the antiviral cocktail allowed the healthy lung epithelial cell population to recover fully by 35 dpi (Fig. 13 (a)). In contrast, the immunosuppressant cocktail with sub-optimal K_d parameters only gave a moderate, transient decrease in cytokine storm inflammation while making minimal impact on autoimmunity (Figs. 13 (c) and (d)). Consequently, the healthy cell number only recovered to a value of 0.54 n.u., almost half of the homeostatic value of 1 n.u., indicating severe lung damage or death (Fig. 13 (a)). To completely reverse the cytokine storm (Fig. 13 (c)), partially reverse the autoimmune response (Fig. 13 (d)), and match the healthy lung epithelial cell recovery of the antiviral cocktail (Fig. 13 (a)), the immunosuppressant cocktail required full-efficacy (literature K_d) drug performance. Together, these results emphasize the model's prediction that treatment with antivirals early in the disease course is more effective than later treatment with immunosuppressants when trying to avoid cytokine storm or autoimmunity. The full dynamics of all states for the evaluation of cocktails against cytokine storm and adaptive autoimmunity complications are given in Fig. S-13.

X. Conclusion

Using SARS-CoV-2 as a concrete example, this study presents an electronic circuit model of within-host infection kinetics, immune responses, and therapeutic drug interventions, as monotherapies and combination therapy cocktails. The model fits clinical data across disease severities and accounts for the effects of age, sex, and viral variant on COVID-19 dynamics. The model additionally emulates cytokine storm, adaptive autoimmunity, and adaptive immune memory. Several key results were uncovered by running simulations of our model: First, antiviral drugs should be given early to prevent the generation of viral load and inflammatory immune responses later in the disease course. Second, there is a critical tradeoff in the timing of administration of immunosuppressants. Immunosuppressant treatment given too early in the disease course allows for viral load to grow uncontrollably while immunosuppressant treatment given too late will miss the period of peak inflammation, during which immunosuppression is most needed. Third, combining drugs within and across classes (i.e., antivirals and immunosuppressants) has

a larger, synergistic effect on the system compared to monotherapies. Fourth, antiviral drugs administered earlier in the disease course are better for avoiding cytokine storm or autoimmunity than immunosuppressant drugs administered later in the disease course.

In a SARS-CoV-2 pandemic context, the circuit model is significant because it provides a way to rapidly and rationally evaluate the timing, dose, and combination of drugs in a model specific to patient (age, sex) and virus (variant) characteristics. In the future, we envision the model to be a useful platform applicable to other diseases due to its six-state simplicity while robustly capturing host-pathogen-drug interactions. Narrowly interpreted, the model could easily and quickly be applied to future coronavirus or other viral pandemics with different parameters specific to the disease and virus. More broadly, host-pathogen interaction models can also be adapted to represent infectious-disease dynamics where the pathogen is not necessarily viral but could be bacterial or fungal. Most broadly, the model could be adapted for carcinogenesis modeling and cancer cocktail therapy evaluation: in the latter case, the model states would be healthy and cancerous tissue, tumor antigens and circulating cancer cells, and the innate and adaptive immune responses.

For the SARS-CoV-2 circuit model, there are several avenues of further research available. Fitting clinical data from individual patients would provide insight into the infection-to-infection variation in COVID-19 dynamics and model parameters. If data fitting in individual patients is found to be reliable and the ranges of model parameters are well understood, the model may be able to make personalized drug cocktail formulation suggestions for patients. Also, the production and consumption or degradation rates of the states could be analyzed in terms of their energy costs, allowing for the calculation of power consumption by competing viral and host processes. For example, the transcriptional and translational energy costs to a host cell to produce one virion could be calculated and drugs could be selected that preferentially target metabolically stressed cells. Furthermore, the software-designed-and-run model presented here could be ported to cytomorphic computing chips [1], [4], [53], [88], [89], [90], [91], [92], allowing for high-speed iterations of drug cocktail formulations, which could be optimized by machine learning. Such computational techniques may prove faster than empirical methods at identifying promising drug cocktails for clinical applications. Finally, any of these avenues of further research may identify model parameters that SARS-CoV-2 is highly sensitive to, which can be used to propose new targets for drug discovery efforts.

Using only 6 main states made parametrizing the COVID-19 circuit model tractable, but also gave rise to some of its limitations. Generally, lumping innate and adaptive immunity into just two states made it impossible to capture the responses of different immune cell types and signaling molecules within those systems. In future work, the immunity states could be more granular, separating the adaptive immune response into B- and T-cell populations and separating the innate immune response into phagocytic cell counts and cytokine/chemokine production. A more specific limitation of using a simplified model was that drugs' mechanisms of action become oversimplified. For example, Toc is a mAb that targets the IL-6 receptor, but many other cytokines exist and likely contribute to cytokine storms [93]. Yet, the model groups all of these cytokines, and Toc's effect on them, into a single innate immunity state variable. This loss of drug mechanism and target specificity

may have also contributed to the model's failure to differentiate the performance of Mol and Pax; in reality, Pax has outperformed Mol in clinical trials [25], [26]. It is also possible that the modeled Mol-Pax similarity arose from bioavailability or saturation constant parameters being incompletely examined in the literature or from the absence of viral variant effects on drug efficacies in the model. In future models of drug effects, the drug targets could be modeled with greater mechanistic detail before being connected back into the rest of the biological system.

In conclusion, we have developed a circuit model of virus-host-drug interactions in COVID-19 that fits clinical data and accounts for key host (age, sex, immunological memory), virus (variant), and disease (severity, complications) features. The model allows us to make predictions about which drug regimens and combinations can best combat infection and reduce the risk of complications.

Circuit models, which are quantitative yet visually tractable, are a useful tool to gain insight into biological systems and are an enabling tool for drug-cocktail formulation and design.

Supplementary Material

Refer to Web version on PubMed Central for supplementary material.

Acknowledgments

This work was supported in part by the Air Force Office of Scientific Research (AFOSR) under Grant FA9550-18-1-0467; in part by the National Institutes of Health under Grant R01 GM 123032-01; and in part by Dartmouth College.

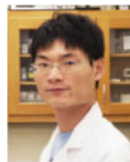
Biographies



Douglas Raymond Beahm received the Bachelor of Arts degree in engineering in 2019 and the Bachelor of Engineering degree from the Thayer School of Engineering, Dartmouth College, Hanover, NH, USA, where he is currently pursuing the Ph.D. degree with the Sarpeshkar Lab, focusing on circuit models of biological systems.

Previously, he was a Research Assistant with Sarpeshkar Lab, Thayer School of Engineering, and a Research & Early Development Intern with IDEXX Laboratories, Westbrook, ME, USA.

Mr. Beahm is a member of the Tau Beta Pi Engineering Honors Society.



Yijie (Daniel) Deng received the B.S. degree in pharmaceutical engineering from Fuzhou University, Fuzhou, China, the master's degree in biochemical engineering from Shenyang Pharmaceutical University, Shenyang, China, and the Ph.D. degree from the University of Southern Mississippi, Hattiesburg, MS, USA. He is currently a Research Scientist with Prof. R. Sarpeshkar's Lab, Dartmouth College, Hanover, NH, USA. His research focuses on both fundamental and application studies in synthetic biology, including biological noise, circuit modeling, cell-free biosensor developments, bacterial drug persistence, and protein engineering. Before joining Dartmouth College, he was a Postdoctoral Researcher with the State University of New York (SUNY) University at Buffalo, NY, USA, and Virginia Commonwealth University, Richmond, VA, USA, where he studied the interactions of oral bacteria and human host. His work resulted in multiple impactful publications with over 200 citations and an H-index of 7 at present.



Thomas M. DeAngelo received the B.A. degree (Hons.) in computational biology from Colby College, Waterville, ME, USA, in May 2022. He is currently pursuing the B.E. degree in biomedical engineering from the Thayer School of Engineering, Dartmouth College, Hanover, NH, USA. Since June 2018, he has been a Research Assistant with Dr. L. Walensky with Dana-Farber Cancer Institute, Boston, MA, USA. During his time at Colby, he performed research in the laboratory of Prof. K. Rice. Since May 2021, he has also been working as a Research Assistant for Prof. R. Sarpeshkar with Dartmouth College. His research with Dr. L. Walensky and Prof. K. Rice focused on deregulated apoptotic pathways in cancer. His current and interdisciplinary research with Prof. R. Sarpeshkar aims to highlight the benefits of interweaving medicine with engineering. He received the Colby's Pulver Science Scholar Award in 2019 and a Pediatric Oncology Student Training Award from Alex's Lemonade Stand Foundation in 2020.



Rahul Sarpeshkar (Fellow, IEEE) received the B.S. degree in electrical engineering and physics from the Massachusetts Institute of Technology (MIT), Cambridge, MA, USA, and the Ph.D. degree from the California Institute of Technology, Pasadena, CA, USA. He is

currently the Thomas E. Kurtz Professor with Dartmouth College, Hanover, NH, USA, where he is also a Professor of Engineering, Physics, Microbiology and Immunology, and Molecular and Systems Biology. His research creates novel wet DNA–protein circuits in living cells and also advanced dry nanoelectronic circuits on silicon chips for quantum and biological circuit applications. Before joining Dartmouth’s Faculty, he was a Tenured Professor with MIT, leading the Analog Circuits and Biological Systems Group, Research Laboratory of Electronics. Before joining MIT, he was a member of the Technical Staff of Bell Labs’ Division of Biological Computation, Physics Department. His longstanding work on analog and biological computation and his most recent work have helped pioneer the field of analog synthetic biology. His work on a glucose fuel cell for medical implants was featured by Scientific American among 2012’s 10 World Changing Ideas. He holds 44 awarded patents, has authored multiple publications, including one that was featured on the cover of *Nature*, and has over 13 000 citations and an H-index of 54 at present. His book *Ultra Low Power Bioelectronics: Fundamentals, Biomedical Applications, and Bio-Inspired Systems* (Cambridge University Press, 2010) revealed the deep connections between analog transistor circuits and biochemical circuits and founded the field of cytomorphic systems. His group holds several first or best records in analog, bioinspired, quantum inspired, synthetic biology, medical device, ultra-low-power, and energy harvesting systems. His work has applications in implantable medical devices for those with hearing impairments, low/limited vision, and/or limited mobility, and in biotechnology, medical, or AI applications that benefit from cellular engineering or quantum-inspired engineering. He was a recipient of several awards, including the NSF CAREER Award, the ONR Young Investigator Award, and the Packard Fellows Award. He is a Fellow of the National Academy of Inventors.

References

- [1]. Sarpeshkar R, *Ultra Low Power Bioelectronics: Fundamentals, Biomedical Applications, and Bio-Inspired Systems*, 1st ed. Cambridge, UK: Cambridge Univ. Press, 2010.
- [2]. Sarpeshkar R, “Analog synthetic biology,” *Philos. Trans. Royal Soc. A*, vol. 372, Mar. 2014, Art. no. 20130110, doi: 10.1098/rsta.2013.0110.
- [3]. Teo JJY, Woo SS, and Sarpeshkar R, “Synthetic biology: A unifying view and review using analog circuits,” *IEEE Trans. Biomed. Circuits Syst*, vol. 9, no. 4, pp. 453–474, Aug. 2015, doi: 10.1109/TBCAS.2015.2461446. [PubMed: 26372648]
- [4]. Teo JJY, Weiss R, and Sarpeshkar R, “An Artificial tissue homeostasis circuit designed via analog circuit techniques,” *IEEE Trans. Biomed. Circuits Syst*, vol. 13, no. 3, pp. 540–553, Jun. 2019, doi: 10.1109/TBCAS.2019.2907074. [PubMed: 30908238]
- [5]. Teo JJY and Sarpeshkar R, “The merging of biological and electronic circuits,” *iScience*, vol. 23, no. 11, Nov. 2020, Art. no. 101688, doi: 10.1016/j.isci.2020.101688.
- [6]. Deng Y, Beahm DR, Ran X, Riley TG, and Sarpeshkar R, “Rapid modeling of experimental molecular kinetics with simple electronic circuits instead of with complex differential equations,” *Front. Bioeng. Biotechnol*, vol. 10, Sep. 2022, Art. no. 947508, doi: 10.3389/fbioe.2022.947508.
- [7]. Daniel R, Rubens JR, Sarpeshkar R, and Lu TK, “Synthetic analog computation in living cells,” *Nature*, vol. 497, pp. 619–623, May 2013, doi: 10.1038/nature12148. [PubMed: 23676681]
- [8]. Zeng J, Teo J, Banerjee A, Chapman TW, Kim J, and Sarpeshkar R, “A synthetic microbial operational amplifier,” *ACS Synth. Biol*, vol. 7, no. 9, pp. 2007–2013, Aug. 2018, doi: 10.1021/acssynbio.8b00138. [PubMed: 30152993]
- [9]. Deng Y, Beahm DR, Ionov S, and Sarpeshkar R, “Measuring and modeling energy and power consumption in living microbial cells with a synthetic ATP reporter,” *BMC Biol*, vol. 19, p. 101, May 2021, doi: 10.1186/s12915-021-01023-2. [PubMed: 34001118]

- [10]. Bartlett JA et al. , “An updated systematic overview of triple combination therapy in antiretroviral-naive HIV-infected adults,” *AIDS*, vol. 20, no. 16, pp. 2051–2064, Oct. 2006, doi: 10.1097/01.aids.0000247578.08449.ff. [PubMed: 17053351]
- [11]. Mendoza P et al. , “Combination therapy with anti-HIV-1 antibodies maintains viral suppression,” *Nature*, vol. 561, pp. 479–484, Sep. 2018, doi: 10.1038/s41586-018-0531-2. [PubMed: 30258136]
- [12]. Gaebler C et al. , “Prolonged viral suppression with anti-HIV-1 antibody therapy,” *Nature*, vol. 606, pp. 368–374, Apr. 2022, doi: 10.1038/s41586-022-04597-1. [PubMed: 35418681]
- [13]. Koszalka P, Tilmanis D, and Hurt AC, “Influenza antivirals currently in late-phase clinical trial,” *Influenza Other Respi. Viruses*, vol. 11, no. 3, pp. 240–246, Feb. 2017, doi: 10.1111/irv.12446.
- [14]. O’Neil B et al. , “A phase 2 study of pimodivir (JNJ-63623872) in combination with oseltamivir in elderly and nonelderly adults hospitalized with influenza A infection: OPAL study,” *J. Infect. Dis.*, vol. 226, no. 1, pp. 109–118, Jul. 2020, doi: 10.1093/infdis/jiaa376.
- [15]. Deng R et al. , “Pharmacokinetics of the monoclonal antibody MHAA4549A administered in combination with oseltamivir in patients hospitalized with severe influenza A infection,” *J. Clin. Pharmacol.*, vol. 60, no. 11, pp. 1509–1518, Jul. 2020, doi: 10.1002/jcph.1652. [PubMed: 32621543]
- [16]. “WHO coronavirus (COVID-19) dashboard.” World Health Organization. Accessed: Feb. 1, 2023. [Online]. Available: <https://covid19.who.int>
- [17]. Accorsi EK et al. , “Association between 3 doses of mRNA COVID-19 vaccine and symptomatic infection caused by the SARS-CoV-2 Omicron and delta variants,” *JAMA*, vol. 237, no. 7, pp. 639–651, Feb. 2022, doi: 10.1001/jama.2022.0470.
- [18]. Moreira ED et al. , “Safety and efficacy of a third dose of BNT162b2 Covid-19 vaccine,” *New Engl. J. Med.*, vol. 387, no. 20, pp. 1910–1921, May 2022, doi: 10.1056/NEJMoa2200674. [PubMed: 36383726]
- [19]. Johnson AG et al. , “COVID-19 incidence and death rates among unvaccinated and fully vaccinated adults with and without booster doses during periods of delta and omicron variant emergence—25 U.S. Jurisdictions, April 4–December 25, 2021,” *Morb. Mortal. Weekly Rep.*, vol. 71, no. 4, pp. 132–138, Jan. 2022, doi: 10.15585/mmwr.mm7104e2.
- [20]. Ebinger JE et al. , “Demographic and clinical characteristics associated with variations in antibody response to BNT162b2 COVID-vaccination among healthcare workers at an academic medical centre: A longitudinal cohort analysis,” *BMJ Open*, vol. 12, no. 5, May 2022, Art. No. e059994, doi: 10.1136/bmjopen-2021-059994.
- [21]. Feikin DR et al. , “Duration of effectiveness of vaccines against SARS-CoV-2 infection and COVID-19 disease: Results of a systematic review and meta-regression,” *Lancet*, vol. 339, no. 10328, pp. 924–944, Mar. 2022, doi: 10.1016/S0140-6736(22)00152-0.
- [22]. Juthani PV et al. , “Hospitalisation among vaccine breakthrough COVID-19 infections,” *Lancet Infect. Dis.*, vol. 21, no. 11, pp. 1485–1486, Nov. 2021, doi: 10.1016/S1473-3099(21)00558-2. [PubMed: 34506735]
- [23]. Wang SY et al. , “Severe breakthrough COVID-19 cases in the SARSCoV-2 delta (B.1.617.2) variant era,” *Lancet Microbe*, vol. 3, no. 1, pp. E4–E5, Jan. 2022, doi: 10.1016/S2666-5247(21)00306-2. [PubMed: 34901896]
- [24]. Brodin P, “Immune determinants of COVID-19 disease presentation and severity,” *Nat. Med.*, no. 27, pp. 28–33, Jan. 2021, doi: 10.1038/s41591-020-01202-8. [PubMed: 33442016]
- [25]. Bernal AJ et al. , “Molnupiravir for oral treatment of Covid-19 in nonhospitalized patients,” *New Engl. J. Med.*, vol. 386, no. 6, pp. 509–520, Feb. 2022, doi: 10.1056/NEJMoa2116044. [PubMed: 34914868]
- [26]. Hammond J et al. , “Oral nirmatrelvir for high-risk, nonhospitalized adults with Covid-19,” *New Engl. J. Med.*, vol. 386, no. 15, pp. 1397–1408, Apr. 2022, doi: 10.1056/NEJMoa2118542. [PubMed: 35172054]
- [27]. Weinreich DM et al. , “REGEN-COV antibody combination and outcomes in outpatients with Covid-19,” *New Engl. J. Med.*, vol. 385, p. e81, Dec. 2021, doi: 10.1056/NEJMoa2108163. [PubMed: 34587383]

- [28]. Gupta A et al. , “Early treatment for Covid-19 with SARS-CoV-2 neutralizing antibody sotrovimab,” *New Engl. J. Med.*, vol. 385, no. 21, pp. 1941–1950, Nov. 2021, doi: 10.1056/NEJMoa2107934. [PubMed: 34706189]
- [29]. Streinu-Cercel A et al. , “Efficacy and safety of regdanvimab (CTP59): A phase 2/3 randomized, double-blind, placebo-controlled trial in outpatients with mild-to-moderate coronavirus disease 2019,” *Open Forum Infect. Dis.*, vol. 9, no. 4, Feb. 2022, Art. no. ofac053, doi: 10.1093/ofid/ofac053.
- [30]. The RECOVERY Collaborative Group, “Dexamethasone in hospitalized patients with Covid-19” *New Engl. J. Med.*, vol. 384, no. 8, pp. 693–704, Feb. 2021, doi: 10.1056/NEJMoa2021436. [PubMed: 32678530]
- [31]. Tomazini BM et al. , “Effect of dexamethasone on days alive and ventilator-free in patients with moderate or severe acute respiratory distress syndrome and COVID-19: The CoDEX randomized clinical trial,” *JAMA*, vol. 324, no. 13, pp. 1307–1316, Sep. 2020, doi: 10.1001/jama.2020.17021. [PubMed: 32876695]
- [32]. Toroghi N et al. , “Comparing efficacy and safety of different doses of dexamethasone in the treatment of COVID-19: A three-arm randomized clinical trial,” *Pharmacol. Rep.*, vol. 74, no. 1, pp. 229–240, Feb. 2022, doi: 10.1007/s43440-021-00341-0. [PubMed: 34837648]
- [33]. Salvarani C et al. , “Effect of tocilizumab vs standard care on clinical worsening in patients hospitalized with COVID-19 pneumonia: A randomized clinical trial,” *JAMA Internal Med.*, vol. 181, no. 1, pp. 24–31, Oct. 2020, doi: 10.1001/jamainternmed.2020.6615.
- [34]. Stone JH et al. , “Efficacy of tocilizumab in patients hospitalized with Covid-19,” *New Engl. J. Med.*, vol. 383, no. 24, pp. 2333–2344, Dec. 2020, doi: 10.1056/NEJMoa2028836. [PubMed: 33085857]
- [35]. Rosas IO et al. , “Tocilizumab in hospitalized patients with severe Covid-19 pneumonia,” *New Engl. J. Med.*, vol. 384, no. 16, pp. 1503–1516, Apr. 2021, doi: 10.1056/NEJMoa2028700. [PubMed: 33631066]
- [36]. Hermine O, Mariette X, Tharaux PL, Resche-Rigon M, Porcher R, and Ravaud P, “Effect of tocilizumab vs usual care in adults hospitalized with COVID-19 and moderate or severe pneumonia: A randomized clinical trial,” *JAMA Internal Med.*, vol. 181, no. 1, pp. 32–40, Oct. 2020, doi: 10.1001/jamainternmed.2020.6820.
- [37]. Salama C et al. , “Tocilizumab in patients hospitalized with Covid-19 pneumonia,” *New Engl. J. Med.*, vol. 384, no. 1, pp. 20–30, Jan. 2021, doi: 10.1056/NEJMoa2030340. [PubMed: 33332779]
- [38]. Perelson AS and Ke R, “Mechanistic modeling of SARS-CoV-2 and other infectious diseases and the effects of therapeutics,” *Clin. Pharmacol. Ther.*, vol. 109, no. 4, pp. 829–840, Dec. 2020, doi: 10.1002/cpt.2160.
- [39]. Wang S, Pan Y, Wang Q, Miao H, Brown AN, and Rong L, “Modeling the viral dynamics of SARS-CoV-2 infection,” *Math. Biosci.*, vol. 328, Oct. 2020, Art. no. 108438, doi: 10.1016/j.mbs.2020.108438.
- [40]. Gonçalves A et al. , “Timing of antiviral treatment initiation is critical to reduce SARS-CoV-2 viral load,” *CPT Pharmacometr. Syst. Pharmacol.*, vol. 9, no. 9, pp. 509–514, Sep. 2020, doi: 10.1002/psp4.12543.
- [41]. Li C, Xu J, Liu J, and Zhou Y, “The within-host viral kinetics of SARS-CoV-2,” *Math. Biosci. Eng.*, vol. 17, no. 4, pp. 2853–2861, Mar. 2020, doi: 10.3934/mbe.2020159. [PubMed: 32987502]
- [42]. Manisty C et al. , “Time series analysis and mechanistic modelling of heterogeneity and seroreversion in antibody responses to mild SARSCoV-2 infection,” *EBioMedicine*, vol. 65, Mar. 2021, Art. no. 103259, doi: 10.1016/j.ebiom.2021.103259.
- [43]. Prague M, Alexandre M, Thiébaud R, and Guedj J, “Within-host models of SARS-CoV-2: What can it teach us on the biological factors driving virus pathogenesis and transmission?” *Anaesth. Crit. Care Pain Med.*, vol. 41, no. 2, Apr. 2022, Art. no. 101055, doi: 10.1016/j.accpm.2022.101055.
- [44]. Dodd MG, Krishna R, Goncalves A, and Rayner CR, “Model-informed drug repurposing: Viral kinetic modelling to prioritize rational drug combinations for COVID-19,” *Brit. J. Clin. Pharmacol.*, vol. 87, no. 9, pp. 3439–3450, Sep. 2021, doi: 10.1111/bcp.14486. [PubMed: 32693436]

- [45]. Néant N et al. , “Modeling SARS-CoV-2 viral kinetics and association with mortality in hospitalized patients from the French COVID cohort,” *Proc. Nat. Acad. Sci.*, vol. 118, no. 8, Feb. 2021, Art. no. e2017962118, doi: 10.1073/pnas.2017962118.
- [46]. Dogra P et al. , “Innate immunity plays a key role in controlling viral load in COVID-19: Mechanistic insights from a whole-body infection dynamics model,” *ACS Pharmacol. Transl. Sci.*, vol. 4, no. 1, pp. 248–265, Dec. 2020, doi: 10.1021/acspsci.0c00183. [PubMed: 33615177]
- [47]. Fadai NT, Sachak-Patwa R, Byrne HM, Maini PK, Bafadhel M, and Nicolau DV, “Infection, inflammation and intervention: Mechanistic modelling of epithelial cells in COVID-19,” *J. Royal Soc. Interface*, vol. 18, no. 175, Feb. 2021, Art. no. 20200950, doi: 10.1098/rsif.2020.0950.
- [48]. Goyal A, Cardozo-Ojeda EF, and Schiffer JT, “Potency and timing of antiviral therapy as determinants of duration of SARS-CoV-2 shedding and intensity of inflammatory response,” *Sci. Adv.*, vol. 6, no. 47, Nov. 2020, Art. no. eabc7112, doi: 10.1126/sciadv.abc7112.
- [49]. Sego TJ et al. , “A modular framework for multiscale, multicellular, spatiotemporal modeling of acute primary viral infection and immune response in epithelial tissues and its application to drug therapy timing and effectiveness,” *PLoS Comput. Biol.*, vol. 16, no. 12, Dec. 2020, Art. no. e1008451, doi: 10.1371/journal.pcbi.1008451.
- [50]. Voutouri C et al. , “In silico dynamics of COVID-19 phenotypes for optimizing clinical management,” *Proc. Nat. Acad. Sci.*, vol. 118, no. 3, Jan. 2021, Art. no. e2021642118, doi: 10.1073/pnas.2021642118.
- [51]. Ke R, Zitzmann C, Ho DD, Ribeiro RM, and Perelson AS, “In vivo kinetics of SARS-CoV-2 infection and its relationship with a person’s infectiousness,” *Proc. Nat. Acad. Sci.*, vol. 118, no. 49, Dec. 2021, Art. no. e2111477118, doi: 10.1073/pnas.2111477118.
- [52]. Willis MJ, Wright A, Bramfitt V, and Díaz VH, “COVID-19: Mechanistic model calibration subject to active and varying nonpharmaceutical interventions,” *Chem. Eng. Sci.*, vol. 231, Feb. 2021, Art. no. 116330, doi: 10.1016/j.ces.2020.116330.
- [53]. Beahm DR, Deng Y, Riley TG, and Sarpeshkar R, “Cytomorphic electronic systems: A review and perspective,” *IEEE Nanotechnol. Mag.*, vol. 15, no. 6, pp. 41–53, Dec. 2021, doi: 10.1109/MNANO.2021.3113192. [PubMed: 35242267]
- [54]. Wagar LE, Difazio RM, and Davis MM, “Advanced model systems and tools for basic and translational human immunology,” *Genome Med.*, vol. 10, p. 73, Sep. 2018, doi: 10.1186/s13073-018-0584-8. [PubMed: 30266097]
- [55]. Kirschner DE, Hunt CA, Marino S, Fallahi-Sichani M, and Linderman JJ, “Tuneable resolution as a systems biology approach for multi-scale, multi-compartment computational models,” *Wiley Interdiscip. Rev. Syst. Biol. Med.*, vol. 6, no. 4, pp. 289–309, Aug. 2014, doi: 10.1002/wsbm.1270. [PubMed: 24810243]
- [56]. Sarpe V and Jacob C, “Simulating the decentralized processes of the human immune system in a virtual anatomy model,” *BMC Bioinform.*, vol. 14, no. 6, p. S2, Apr. 2013, doi: 10.1186/1471-2105-14-S6-S2.
- [57]. Mitha F, Lucas TA, Feng F, Kepler TB, and Chan C, “The multiscale systems Immunology project: Software for cell-based immunological simulation” *Source Code Biol. Med.*, vol. 3, p. 6, Apr. 2008, doi: 10.1186/1751-0473-3-6. [PubMed: 18442405]
- [58]. Patel BV, Wilson MR, O’Dea KP, and Takata M, “TNF-induced death signaling triggers alveolar epithelial dysfunction in acute lung injury,” *J. Immunol.*, vol. 190, no. 8, pp. 4274–4282, Apr. 2013, doi: 10.4049/jimmunol.1202437. [PubMed: 23487422]
- [59]. Dotan A, Muller S, Kanduc D, David P, Halpert G, and Shoenfeld Y, “The SARS-CoV-2 as an instrumental trigger of autoimmunity,” *Autoimmun. Rev.*, vol. 20, no. 4, Apr. 2021, Art. no. 102792, doi: 10.1016/j.autrev.2021.102792.
- [60]. Wang EY et al. , “Diverse functional autoantibodies in patients with COVID-19,” *Nature*, vol. 595, pp. 283–288, May 2021, doi: 10.1038/s41586-021-03631-y. [PubMed: 34010947]
- [61]. Park JO et al. , “Metabolite concentrations, fluxes and free energies imply efficient enzyme usage,” *Nat. Chem. Biol.*, vol. 12, pp. 482–489, May 2016, doi: 10.1038/nchembio.2077. [PubMed: 27159581]

- [62]. Bennett BD, Kimball EH, Gao M, Osterhout R, Van Dien SJ, and Rabinowitz JD, “Absolute metabolite concentrations and implied enzyme active site occupancy in *Escherichia coli*,” *Nat. Chem. Biol.*, vol. 5, pp. 593–599, Jun. 2009, doi: 10.1038/nchembio.186. [PubMed: 19561621]
- [63]. Borremans B et al. , “Quantifying antibody kinetics and RNA detection during early-phase SARS-CoV-2 infection by time since symptom onset,” *Elife*, vol. 9, Sep. 2020, Art. no. e60122, doi: 10.7554/eLife.60122.
- [64]. Weiss A, Jellingsø M, and Sommer MOA, “Spatial and temporal dynamics of SARS-CoV-2 in COVID-19 patients: A systematic review and meta-analysis,” *EBioMedicine*, vol. 58, Aug. 2020, Art. no. 102916, doi: 10.1016/j.ebiom.2020.102916.
- [65]. Vignali DAA, Collison LW, and Workman CJ, “How regulatory T cells work,” *Nat. Rev. Immunol.*, vol. 8, pp. 523–532, Jul. 2008, doi: 10.1038/nri2343. [PubMed: 18566595]
- [66]. Turner JS et al. , “SARS-CoV-2 infection induces long-lived bone marrow plasma cells in humans,” *Nature*, vol. 595, pp. 421–425, May 2021, doi: 10.1038/s41586-021-03647-4. [PubMed: 34030176]
- [67]. Cohen KW et al. , “Longitudinal analysis shows durable and broad immune memory after SARS-CoV-2 infection with persisting antibody responses and memory B and T cells,” *Cell Rep. Med.*, vol. 2, no. 7, Jul. 2021, Art. no. 100354, doi: 10.1016/j.xcrm.2021.100354.
- [68]. Notarte KI et al. , “Characterization of the significant decline in humoral immune response six months post-SARS-CoV-2 mRNA vaccination: A systematic review,” *J. Med. Virol.*, vol 94, no.7, pp. 2939–2961, Feb. 2022, doi: 10.1002/jmv.27688. [PubMed: 35229324]
- [69]. Biswas M, Rahaman S, Biswas TK, Haque Z, and Ibrahim B, “Association of sex, age, and comorbidities with mortality in COVID-19 patients: A systematic review and meta-analysis,” *Intervirology*, vol. 64, pp. 36–47, Jan. 2021, doi: 10.1159/000512592.
- [70]. Bonanad C et al. , “The effect of age on mortality in patients with COVID-19: A meta-analysis with 611,583 subjects,” *J. Amer. Med. Directors Assoc.*, vol. 21, no. 7, pp. 915–918, Jul. 2020, doi: 10.1016/j.jamda.2020.05.045.
- [71]. Peckham H et al. , “Male sex identified by global COVID-19 meta-analysis as a risk factor for death and ITU admission,” *Nat. Commun.*, vol. 11, p. 6317, Dec. 2020, doi: 10.1038/s41467-020-19741-6. [PubMed: 33298944]
- [72]. McLinden KA, Kranjac D, Deodati LE, Kahn M, Chumley MJ, and Boehm GW, “Age exacerbates sickness behavior following exposure to a viral mimetic,” *Physiol. Behav.*, vol. 105, no. 5, pp. 1219–1225, Mar. 2012, doi: 10.1016/j.physbeh.2011.04.024. [PubMed: 21549726]
- [73]. “Life span as a biomarker.” The Harrison Lab at the Jackson Laboratory. Accessed: May 24, 2022. [Online]. Available: <https://www.jax.org/research-and-faculty/research-labs/the-harrison-lab/gerontology/lifespan-as-a-biomarker>
- [74]. Flurkey K, Curren JM, and Harrison DE, “The mouse in aging research,” in *The Mouse in Biomedical Research*, vol. 3, 2nd ed. Burlington, MA, USA: Academic, 2007, ch. 20.
- [75]. Jabal KA et al. , “Impact of age, ethnicity, sex and prior infection status on immunogenicity following a single dose of the BNT162b2 mRNA COVID-19 vaccine: Real-world evidence from healthcare workers, Israel, December 2020 to January 2021,” *Eurosurveillance*, vol. 26, no. 6, Feb. 2021, Art. no. 2100096, doi: 10.2807/1560-7917.ES.2021.26.6.2100096.
- [76]. Cai Y et al. , “Structural basis for enhanced infectivity and immune evasion of SARS-CoV-2 variants,” *Science*, vol. 373, no. 6555, pp. 642–648, Jun. 2021, doi: 10.1126/science.abi9745. [PubMed: 34168070]
- [77]. Zhang J et al. , “Membrane fusion and immune evasion by the spike protein of SARS-CoV-2 delta variant,” *Science*, vol. 374, no. 6573, pp. 1353–1360, Oct. 2021, doi: 10.1126/science.abl9463. [PubMed: 34698504]
- [78]. Sheikh A, McMenamin J, Taylor B, and Robertson C, “SARS-CoV-2 Delta VOC in Scotland: demographics, risk of hospital admission, and vaccine effectiveness,” *Lancet*, vol. 397, no. 10293, pp. 2461–2462, Jun. 2021, doi: 10.1016/S0140-6736(21)01358-1. [PubMed: 34139198]
- [79]. Paredes MI et al. , “Associations between SARS-CoV-2 variants and risk of COVID-19 hospitalization among confirmed cases in Washington State: A retrospective cohort study,” *Clin. Infect. Dis.*, vol. 75, no. 1, pp. e536–e544, Jul. 2022, doi: 10.1093/cid/ciac279. [PubMed: 35412591]

- [80]. Veneti L et al. , “No difference in risk of hospitalization between reported cases of the SARS-CoV-2 Delta variant and Alpha variant in Norway,” *Int. J. Infect. Dis.*, vol. 115, pp. 178–184, Feb. 2022, doi: 10.1016/j.ijid.2021.12.321. [PubMed: 34902584]
- [81]. Voss JD et al. , “Variants in SARS-CoV-2 associated with mild or severe outcome,” *Evol. Med. Public Health*, vol. 9, no. 1, pp. 267–275, Jun. 2021, doi: 10.1093/emph/eoab019. [PubMed: 34447577]
- [82]. Nakamichi K et al. , “Hospitalization and mortality associated with SARS-CoV-2 viral clades in COVID-19,” *Sci. Rep.*, vol. 11, no. 1, p. 4802, Feb. 2021, doi: 10.1038/s41598-021-82850-9. [PubMed: 33637820]
- [83]. Thorne LG et al. , “Evolution of enhanced innate immune evasion by SARS-CoV-2,” *Nature*, vol. 602, pp. 487–495, Dec. 2021, doi: 10.1038/s41586-021-04352-y [PubMed: 34942634]
- [84]. Coutinho AE and Chapman KE, “The anti-inflammatory and immunosuppressive effects of glucocorticoids, recent developments and mechanistic insights,” *Mol. Cell Endocrinol.*, vol. 335, no. 1, pp. 2–13, Mar. 2011, doi: 10.1016/j.mce.2010.04.005. [PubMed: 20398732]
- [85]. Kino T, Burd I, and Segars JH, “Dexamethasone for severe Covid-19: How does it work at cellular and molecular levels?” *Int. J. Mol. Sci.*, vol. 22, no. 13, p. 6764, Jun. 2021, doi: 10.3390/ijms22136764. [PubMed: 34201797]
- [86]. Gobbi F et al. , “Antibody response to the bnt162b2 mRNA Covid-19 vaccine in subjects with prior SARS-COV-2 infection,” *Viruses*, vol. 13, no. 3, p. 422, Mar. 2021, doi: 10.3390/v13030422. [PubMed: 33807957]
- [87]. Morales-Núñez JJ, “Neutralizing antibodies titers and side effects in response to BNT162B2 vaccine in healthcare workers with and without prior SARS-CoV-2 infection,” *Vaccines*, vol. 9, no. 7, p. 742, Jul. 2021, doi: 10.3390/vaccines9070742. [PubMed: 34358158]
- [88]. Mandal S and Sarpeshkar R, “Circuit models of stochastic genetic networks,” in *Proc. IEEE Biomed. Circuits Syst. Conf.*, Beijing, China, 2009, pp. 109–112, doi: 10.1109/BIOCAS.2009.5372073.
- [89]. Daniel R, Woo SS, Turicchia L, and Sarpeshkar R, “Analog transistor models of bacterial genetic circuits,” in *Proc. IEEE Biomed. Circuits Syst. Conf.*, San Diego, CA, USA, 2011, pp. 333–336, doi: 10.1109/BioCAS.2011.6107795.
- [90]. Woo SS, Kim J, and Sarpeshkar R, “A cytomorphic chip for quantitative modeling of fundamental bio-molecular circuits,” *IEEE Trans. Biomed. Circuits Syst.*, vol. 9, no. 4, pp. 527–542, Aug. 2015, doi: 10.1109/TBCAS.2015.2446431. [PubMed: 26292344]
- [91]. Kim J, Woo SS, and Sarpeshkar R, “Fast and precise emulation of stochastic biochemical reaction networks with amplified thermal noise in silicon chips,” *IEEE Trans. Biomed. Circuits Syst.*, vol. 12, no. 2, pp. 379–389, Apr. 2018, doi: 10.1109/TBCAS.2017.2786306. [PubMed: 29570064]
- [92]. Woo SS, Kim J, and Sarpeshkar R, “A digitally programmable cytomorphic chip for simulation of arbitrary biochemical reaction networks,” *IEEE Trans. Biomed. Circuits Syst.*, vol. 12, no. 2, pp. 360–378, Apr. 2018, doi: 10.1109/TBCAS.2017.2781253. [PubMed: 29570063]
- [93]. Mulchandani R, Lyngdoh T, and Kakkar AK, “Deciphering the COVID-19 cytokine storm: Systematic review and meta-analysis,” *Eur. J. Clin. Invest.*, vol. 51, no. 1, Oct. 2020, Art. no. e13429, doi: 10.1111/eci.13429.

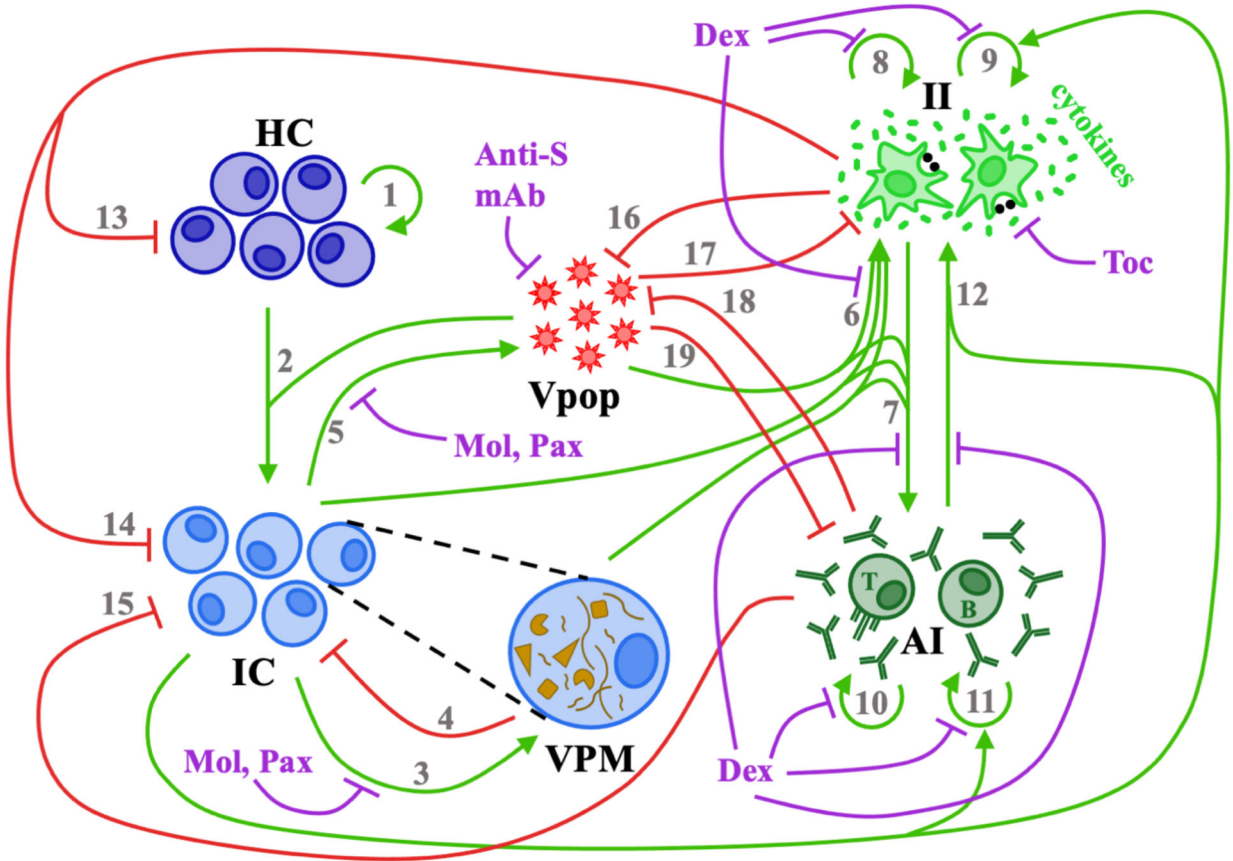


Fig. 1. Flow diagram of the essential interactions between virus, host, and drugs in the circuit model. Positive, upregulating interactions are shown by green lines with activation arrows. Negative, downregulating interactions are shown by red lines with repression symbols except for drugs, which are differentiated by purple lines and repression symbols. The gray numbers marking the interactions correspond to the numbered descriptions of the interactions in the preceding text. Healthy lung epithelial cell number (HC); infected lung epithelial cell number (IC); extracellular viral population virion number (Vpop); intracellular viral protein and molecule number (VPM); the strength of the innate immune response (II); and the strength of the adaptive immune response (AI).

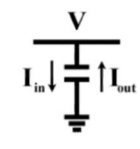
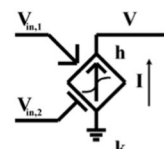
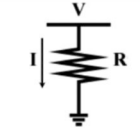
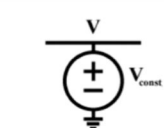
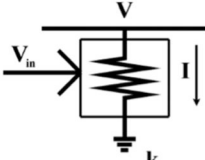
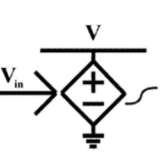
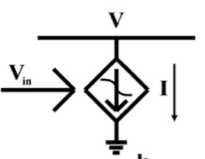
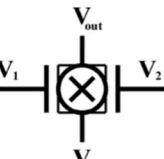
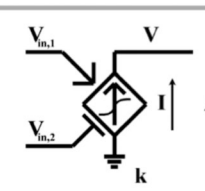
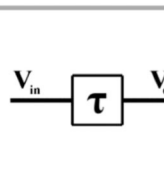
 $\frac{dV}{dt} = I_{in} - I_{out}$	<p>Capacitors accumulate production and degradation rates (currents) to calculate the change in state (voltage) over time.</p>	 $I = k \frac{\left(\frac{V_{in,1}}{K_{d,1}}\right)^h}{1 + \left(\frac{V_{in,1}}{K_{d,1}}\right)^h + \frac{V_{in,2}}{K_{d,2}}}$	<p>Non-linear Hill coefficient current sources make the activating state's effect less gradual around $V_{in,1} = K_{d,1}$.</p>
 $I = \frac{V}{R}$	<p>Resistors degrade the state at a rate proportional to the state and inversely proportional to the resistance.</p>	 $V = V_{const}$	<p>Constant voltage sources fix the state to a constant value.</p>
 $I = kV \frac{\frac{V_{in}}{K_d}}{1 + \frac{V_{in}}{K_d}}$	<p>Non-linear resistors give a second state (V_{in}) saturating control over the otherwise proportional degradation of the main state (V).</p>	 $V = \frac{V_{in}}{1 + \frac{V_{in}}{K_d}}$	<p>Non-linear voltage sources set the main state (V) to a value on $[0,1]$ based on the saturation of the input state (V_{in}).</p>
 $I = k \frac{\frac{V_{in}}{K_d}}{1 + \frac{V_{in}}{K_d}}$	<p>Non-linear current sinks give a second state (V_{in}) saturating control over the otherwise constant degradation of the main state (V).</p>	 $V_{out} = V_{in} \frac{1}{1 + \frac{V_1}{K_{d,1}} + \frac{V_2}{K_{d,2}}}$	<p>Binding blocks determine how much of the total input (V_{in}) is free (V_{out}) after binding with two other species (V_1, V_2).</p>
 $I = k \frac{\frac{V_{in,1}}{K_{d,1}}}{1 + \frac{V_{in,1}}{K_{d,1}} + \frac{V_{in,2}}{K_{d,2}}}$	<p>Two-input non-linear current sources create saturating competition between an activating state ($V_{in,1}$) and a repressing state ($V_{in,2}$) for control of producing the main state (V).</p>	 $\frac{dV_{out}}{dt} = kV_{in} - \frac{V_{out}}{\tau}$	<p>RC filters create an output state that has gain (multiplication of magnitude) and phase (time shift) differences from the input.</p>

Fig. 2. Key conversions between electronic circuit components and mathematical equations. The state variables are represented by voltages, denoted V , and the rate-of-change variables are represented by currents, denoted I . Saturation constants are denoted K_d and cooperativity constants are denoted h .

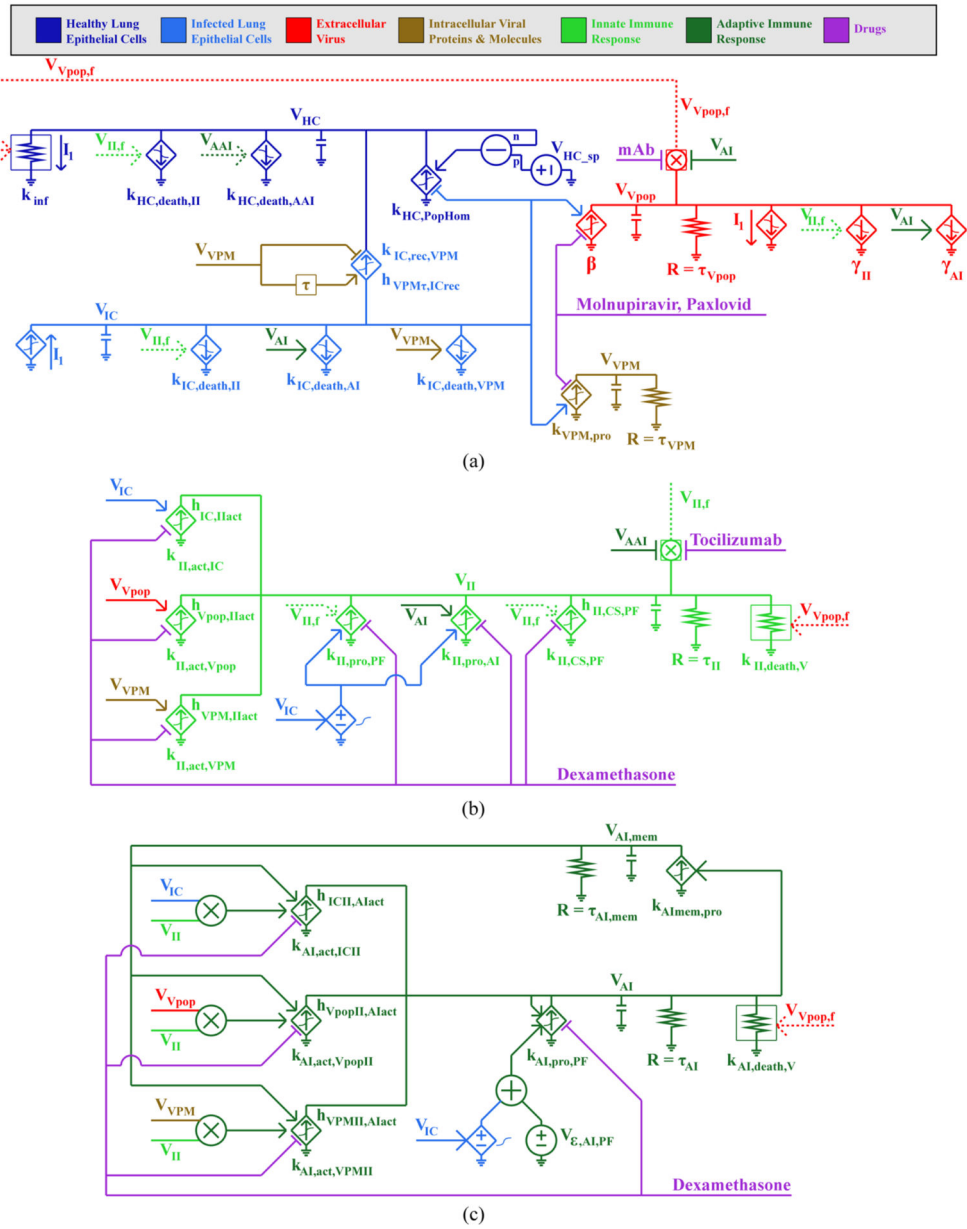
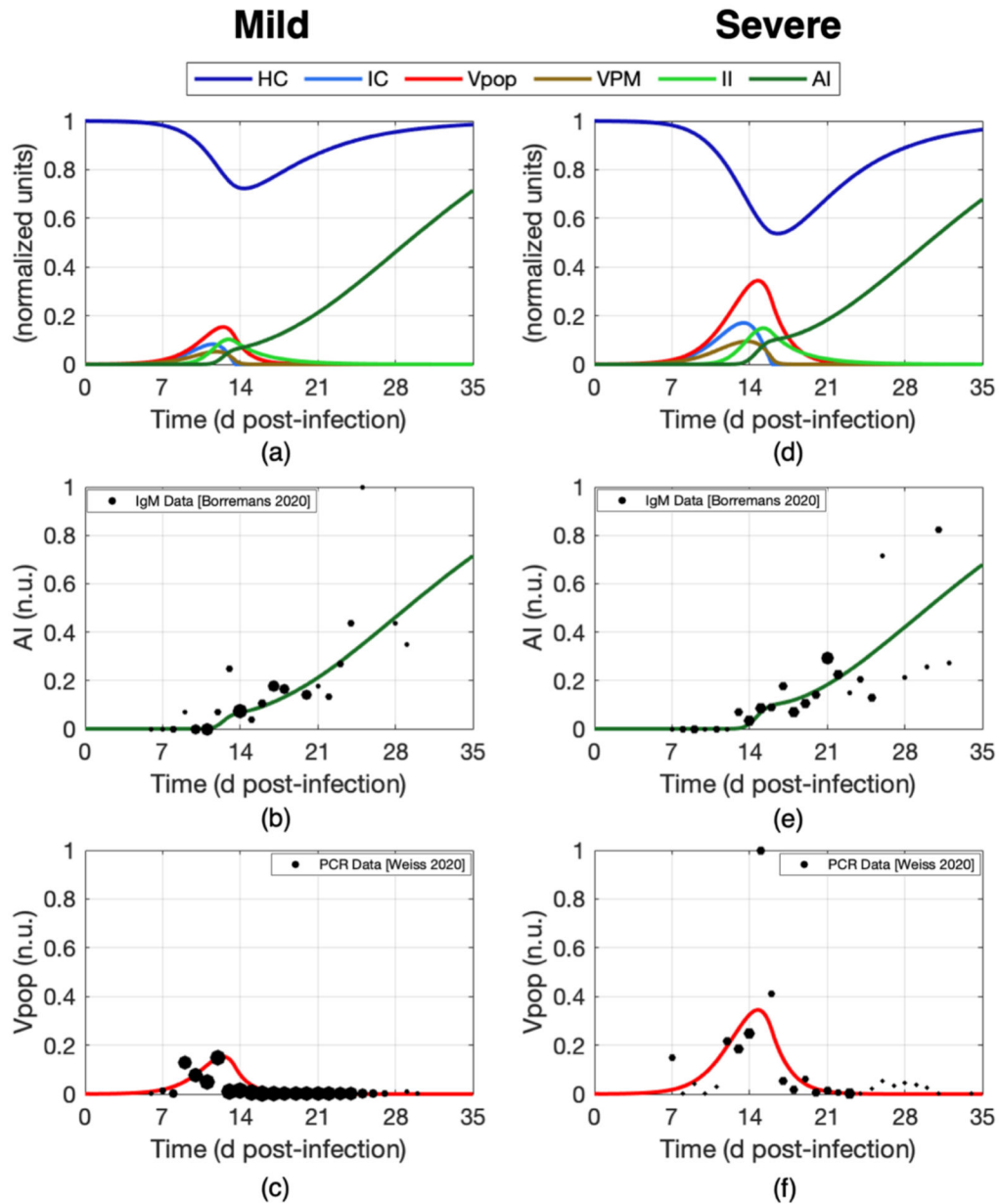


Fig. 3. Electronic circuit schematics of COVID-19. The circuits represent (a) viral replication and infection of lung epithelial cells, (b) the innate immune response, and (c) the adaptive immune response. The states were named V_{HC} for healthy lung epithelial cell number, V_{IC} for infected lung epithelial cell number, V_{Vpop} for extracellular viral population virion number, V_{VPM} for intracellular viral protein and molecule number, V_{II} for the strength of the innate immune response, V_{AI} for the strength of the adaptive immune response, and V_{AAI} for the strength of the adaptive autoimmune response. Wires with the same voltage label are assumed to be connected (i.e., have the same voltage). The wire styles differentiate total (solid lines) and free (dashed lines) variables.

**Fig. 4.**

Dynamics of the COVID-19 circuit model and fits to clinical data for mild and severe disease. (a) The dynamics of the six main model states in a simulation of mild disease. (b) The adaptive immune response strength, AI, from the model agrees with the dynamics of the normalized median level of anti-S IgM antibodies from clinical data for mild disease [63]. (c) The extracellular viral load, Vpop, from the model agrees with the dynamics of normalized clinical PCR measurements from clinical data in mild disease [64]. (d)-(f) The corresponding model dynamics and clinical data fits for severe disease. The only parameters that differ between the mild and severe disease simulations are the immune response activation K_d values, given in Table S-I.c. The data point size is proportional to the number of samples at that time point. The sample size ranges from 1 to 10 for PCR data and

from 1 to 8 for IgM data. See Method S-B for more information about the fitted data. The fitted data is available in the Supplementary Data.

Author Manuscript

Author Manuscript

Author Manuscript

Author Manuscript

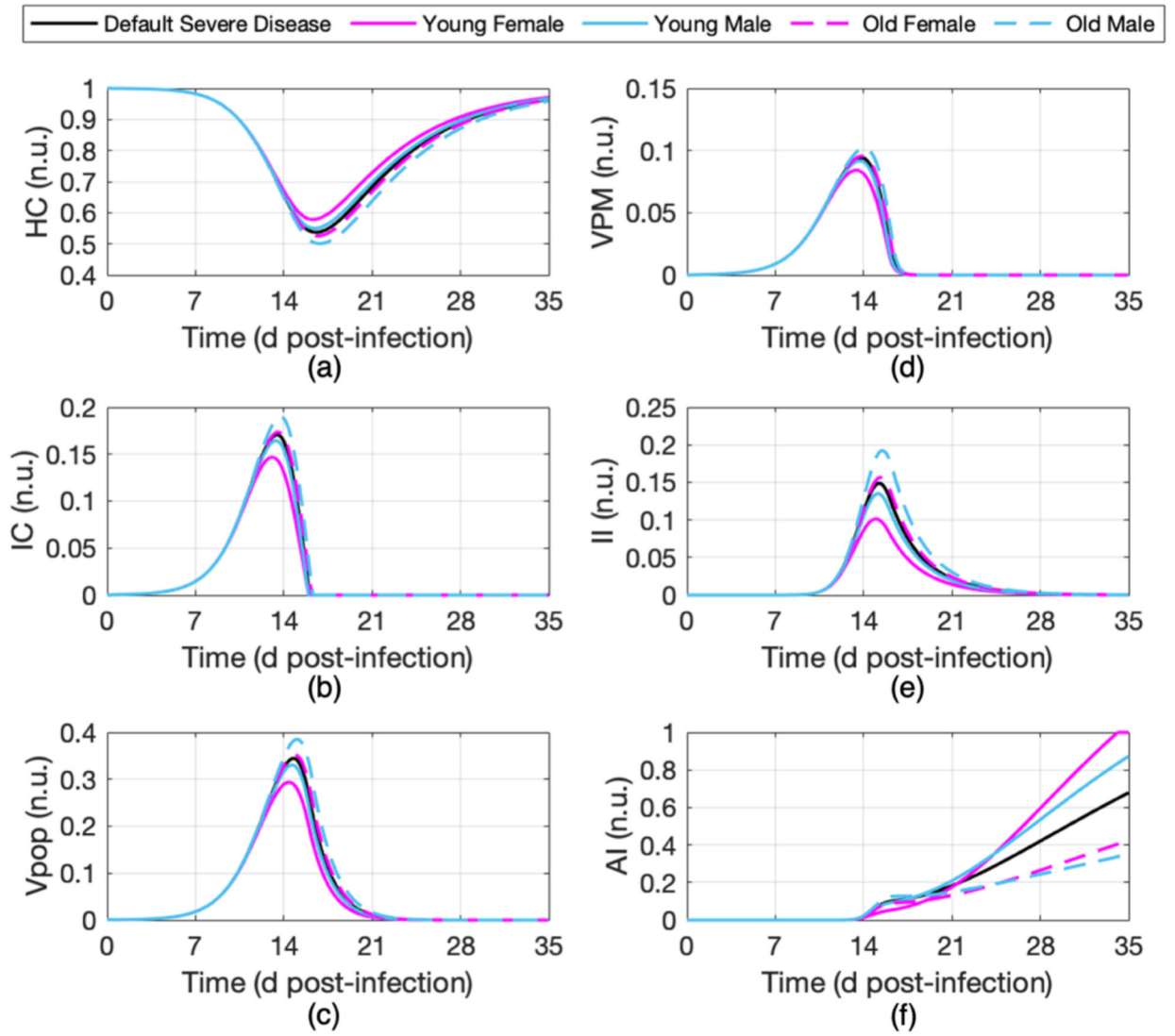
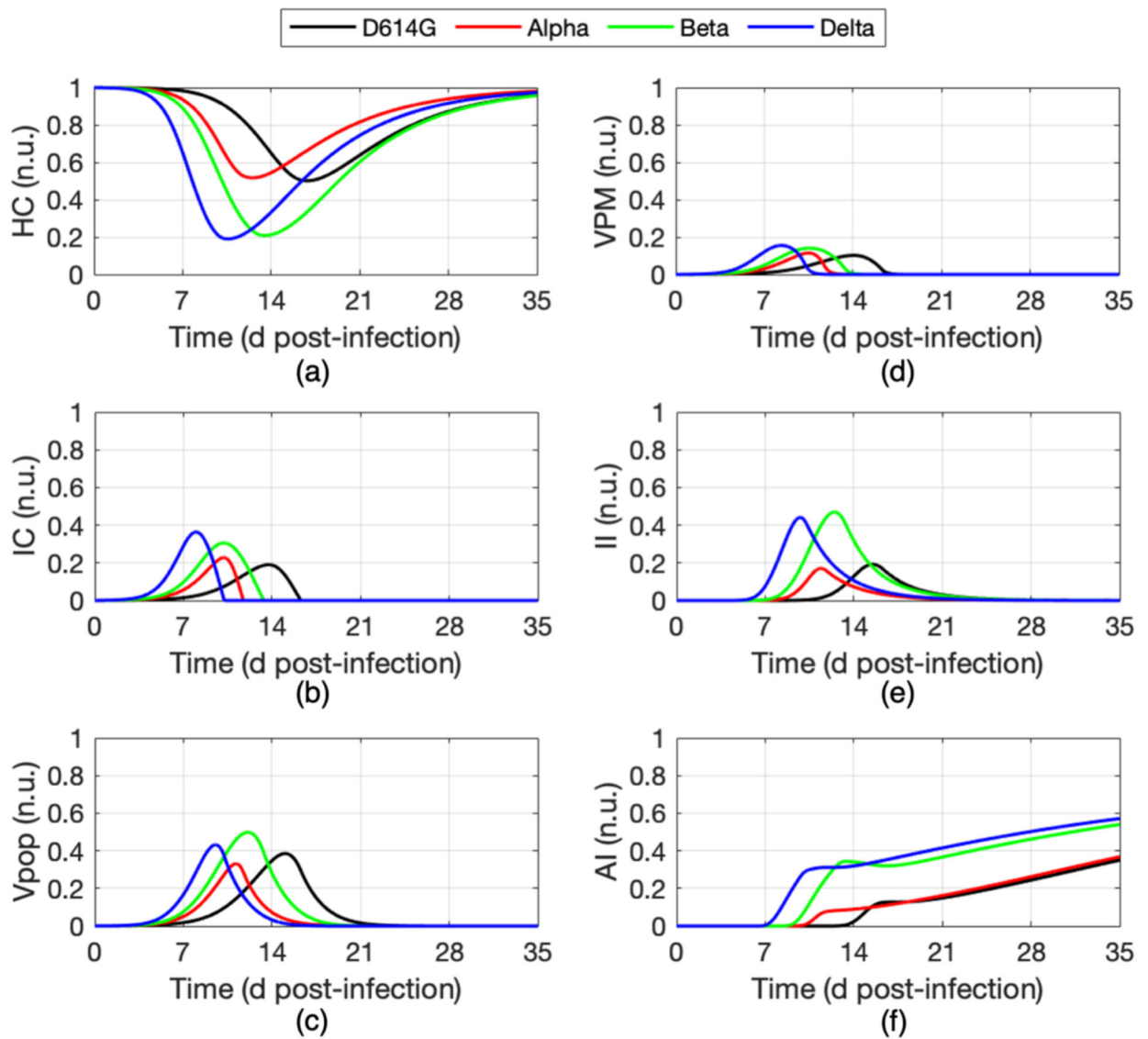


Fig. 5. The effects of age and sex on COVID-19 dynamics. Combinations of age and sex affect all states of the COVID-19 circuit model: (a) healthy lung epithelial cell number (HC), (b) infected lung epithelial cell number (IC), (c) extracellular virion number (Vpop), (d) intracellular viral protein and molecule number (VPM), (e) innate immunity response strength (II), and (f) adaptive immunity response strength (AI). The “Default Severe Disease” curves are identical to the severe disease curves presented in Figs. 4 (d) and (e). Severe disease is assumed for all age and sex combinations.

**Fig. 6.**

The effect of SARS-CoV-2 variants on COVID-19 dynamics. Viral variant type affects all states of the COVID-19 circuit model: (a) healthy lung epithelial cell number (HC), (b) infected lung epithelial cell number (IC), (c) extracellular virion number (Vpop), (d) intracellular viral protein and molecule number (VPM), (e) innate immunity response strength (II), and (f) adaptive immunity response strength (AI). The D614G curves are identical to the old male curves in Fig. 5 and an old male with severe disease is assumed for all viral variant simulations.

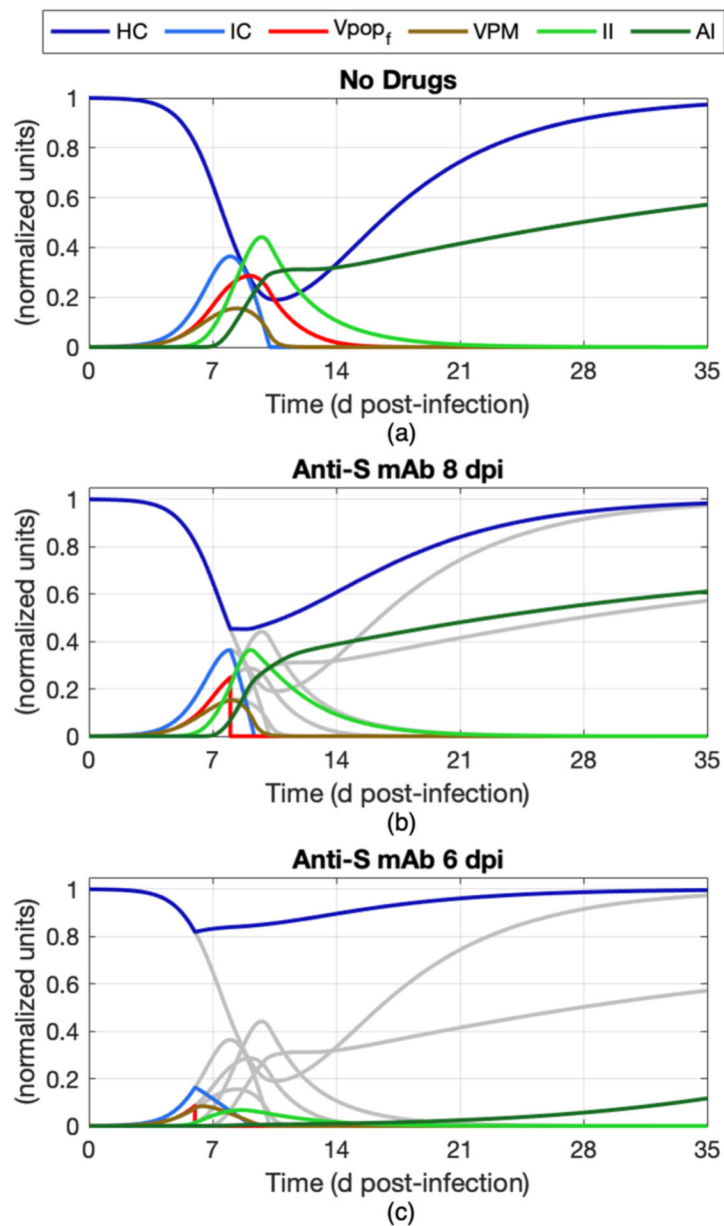
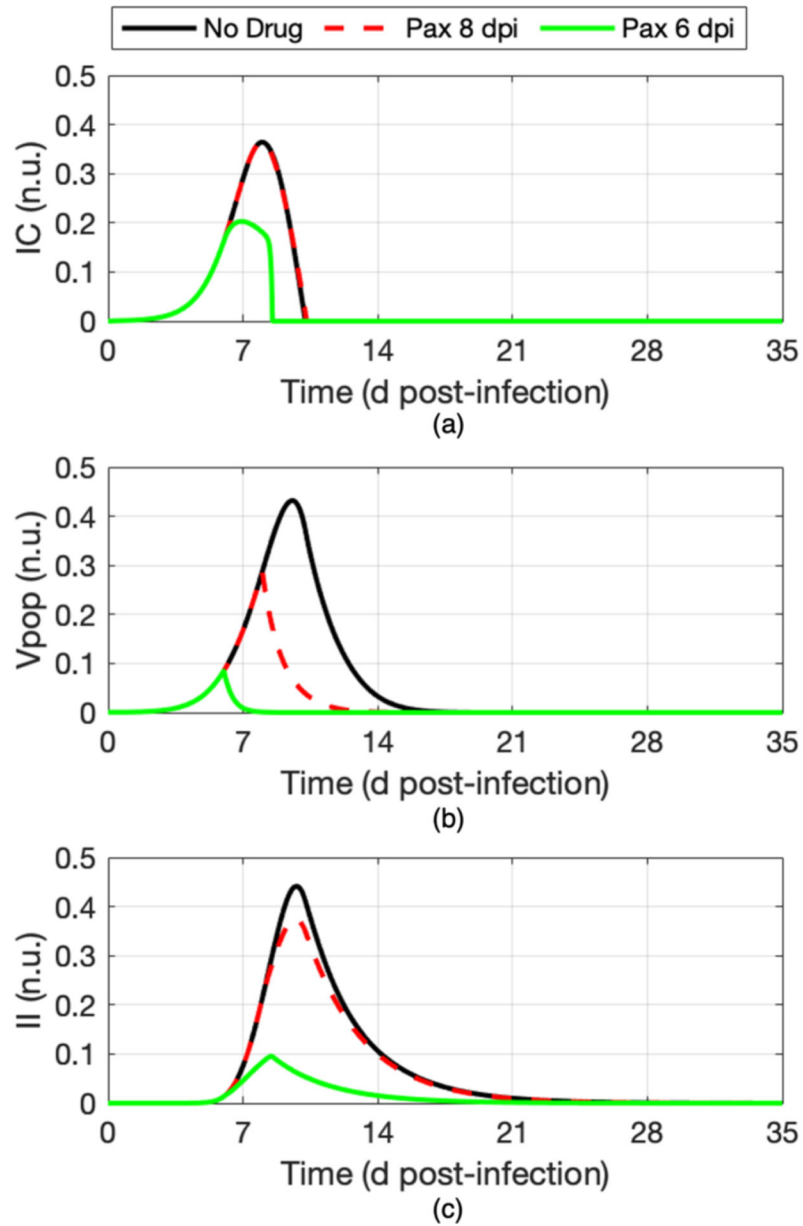


Fig. 7. Anti-S mAb treatment start time optimization via circuit model simulations. Compared to the undrugged simulation (a) and the later 8 dpi treatment in (b), the anti-S mAb monotherapy given at 6 dpi (b) was most effective, causing IC, V_{pop} , and VPM to rapidly go to zero while preserving 80% of the healthy cell population. For ease of comparison, the drugged simulations in (b) and (c) are overlaid on top of the undrugged simulation from (a), represented by gray lines. The simulations assumed severe disease, old age, male sex, and Delta variant.

**Fig. 8.**

Pax treatment start time optimization via circuit model simulations. The latest guidance-given start time of 8 days post-infection (dpi), equivalent to 5 days post-symptom onset in severe disease, reduced the viral load (b), but failed to make significant changes to the number of infected cells (a) or the level of inflammation (c). Administering Pax at the earlier 6 dpi start time reduced all three states: IC, Vpop, and II. The simulations assume severe disease, old age, male sex, and Delta variant.

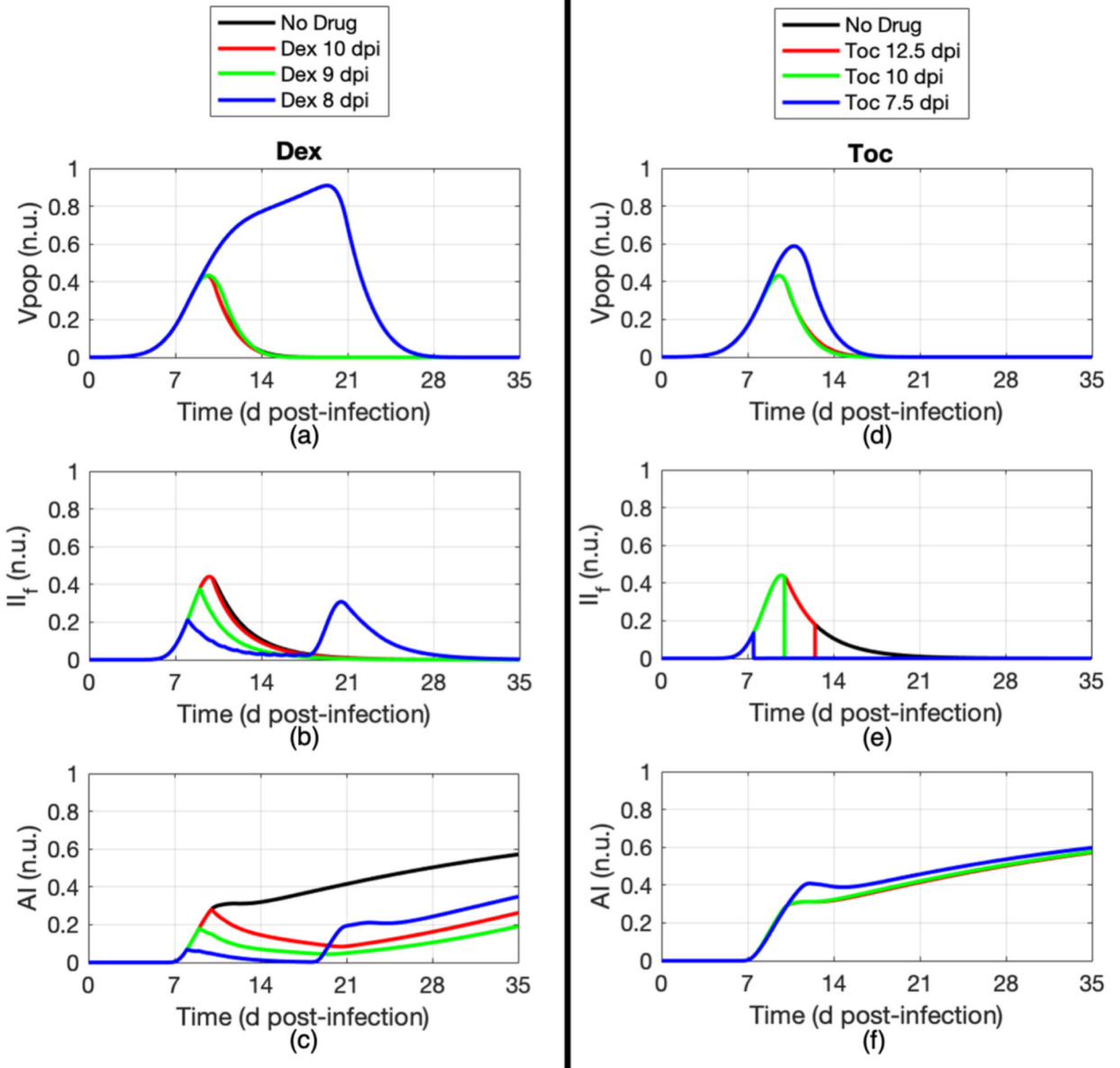


Fig. 9. Dex and Toc monotherapy start time optimization via circuit model simulations. The V_{pop} (a, d), I_f (b, e), and AI (c, f) state dynamics for three different treatment start times for Dex (a)-(c) and Toc (d)-(f) monotherapies suggest that there is an optimal intermediate start time for immunosuppressants that balances viral load management and inflammation reduction. (a) In the worst case, viral load became uncontrollable if Dex was started at 8 dpi because the immunosuppressant was given before the innate and adaptive immune responses were strong enough to stabilize the viral load. In panels in which it cannot be seen, the black line is behind the red line. The simulations assumed severe disease, old age, male sex, and Delta variant.

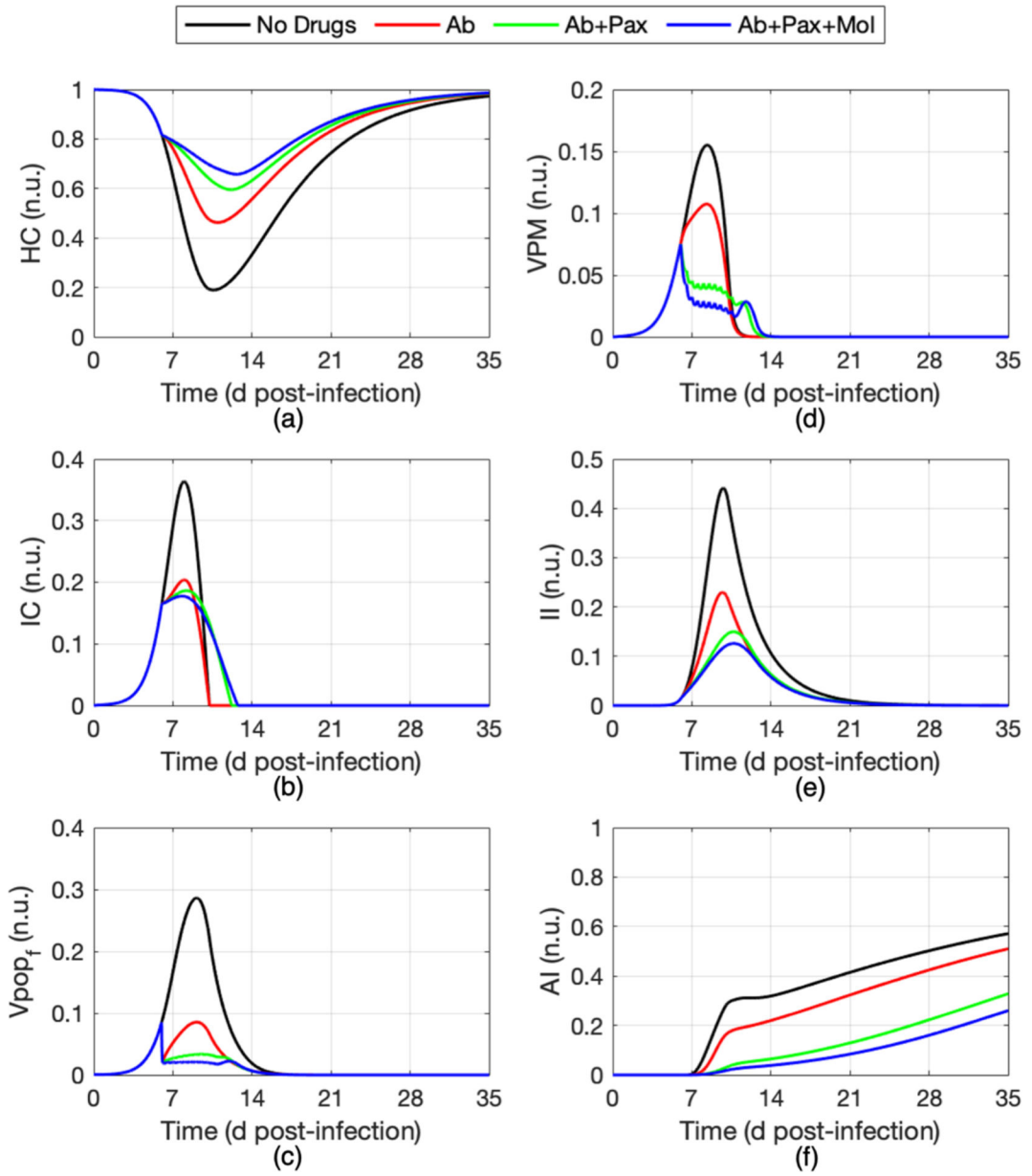


Fig. 10. Model-predicted effects of synergistic antiviral drug cocktails on COVID-19 dynamics. To examine the effect of each component of the antiviral drug cocktail, simulations were run by adding one drug to the cocktail at a time and comparing the resulting changes to state dynamics. The wavy features in some of the plots arise from the frequent dosing and short half-lives of Pax and Mol. All three drugs' start times were 6 dpi. The simulations assumed severe disease, old age, male sex, Delta variant, and high drug K_d values.

Author Manuscript

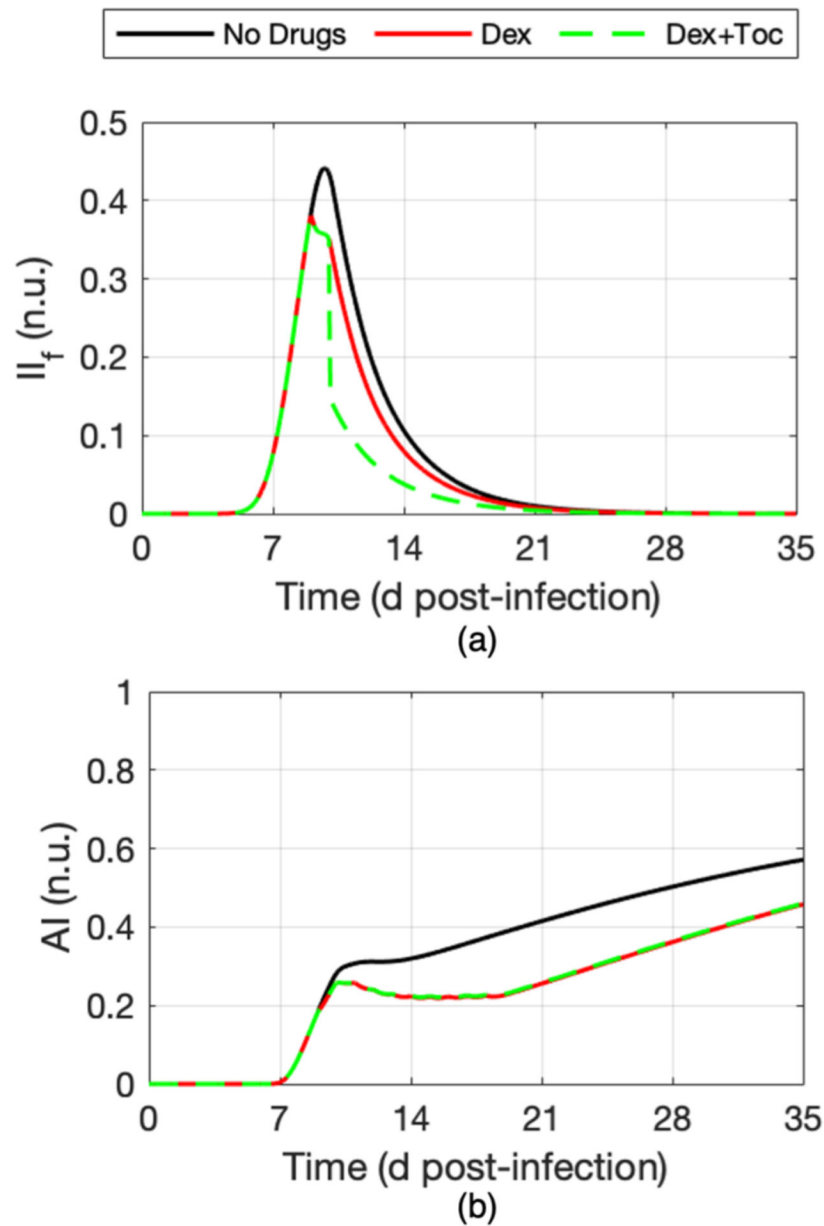


Fig. 11. Model-predicted effects of a synergistic immunosuppressant drug cocktail on COVID-19 dynamics. Dex reduced the peak innate immunity inflammation value (a) at the cost of weakening the adaptive immune response (b). The addition of Toc caused the inflammation to recede from its peak value more quickly (a) without further worsening the adaptive immune response (b). Dex treatment is started at 9 dpi and Toc treatment is started at 10 dpi. The simulations assumed severe disease, old age, male sex, Delta variant, and high drug K_d values.

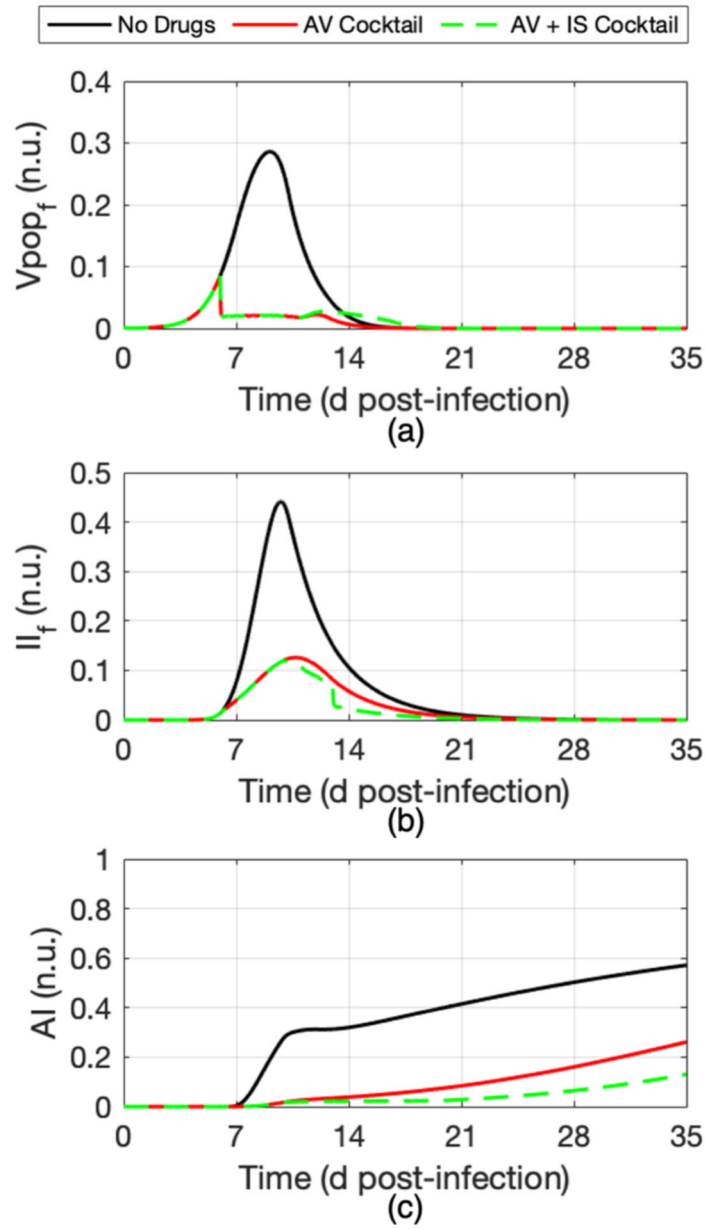


Fig. 12. Model-predicted effects of a synergistic multi-class drug cocktail on COVID-19 dynamics. The antiviral (AV) cocktail greatly reduced the viral load (a), causing a decrease in innate (b) and adaptive (c) immune responses. Adding the immunosuppressant (IS) cocktail to create a multi-class cocktail further reduced the peak level of inflammation and the period of high inflammation (b) at the cost of a longer tail of viral load (a) and a weaker adaptive immune response (c). All three antiviral drugs were started at 6 dpi. Dex treatment was started at 10 dpi and Toc treatment was started at 13 dpi. The simulations assumed severe disease, old age, male sex, Delta variant, and high drug K_d values.

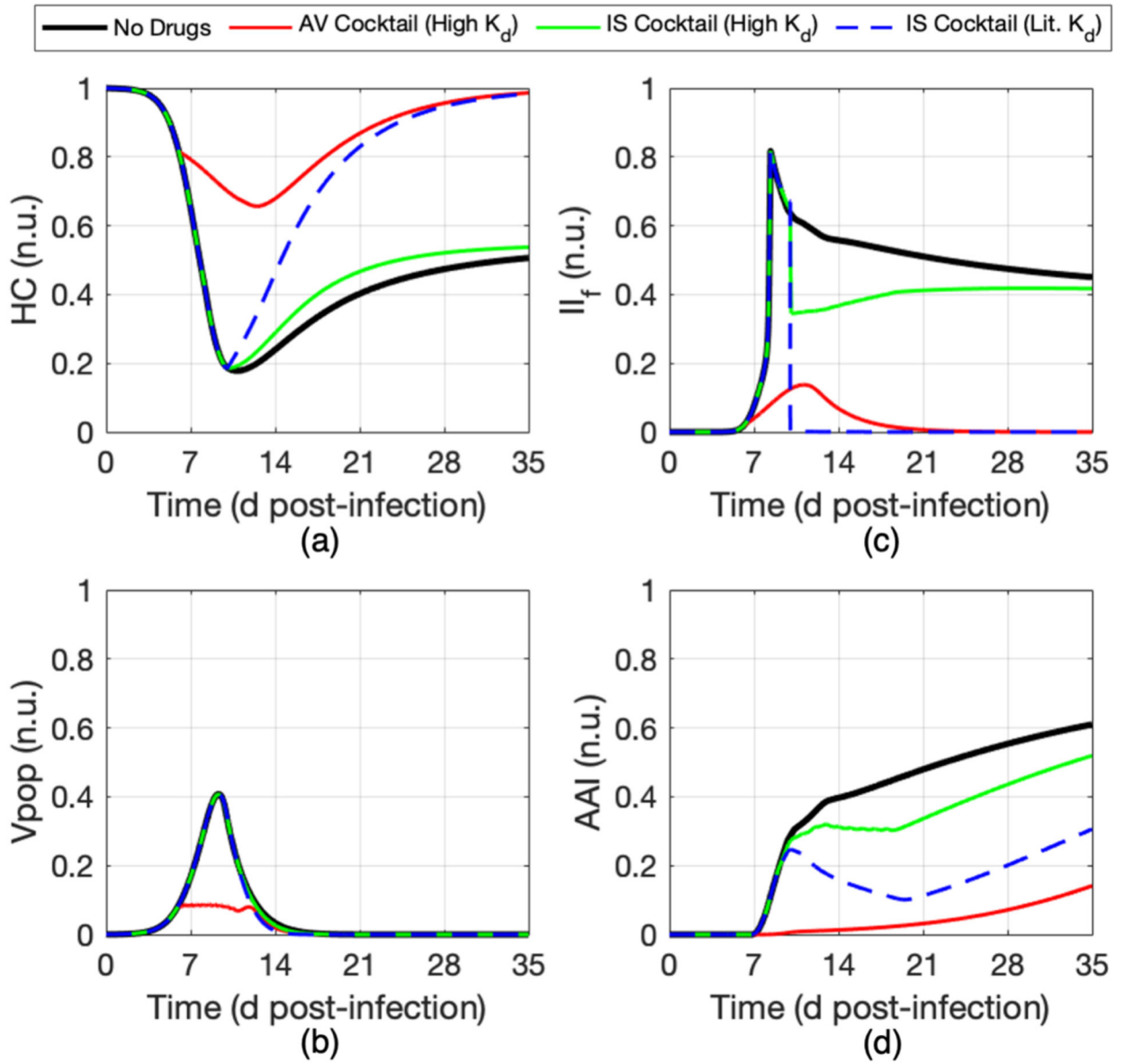


Fig. 13. Antiviral (AV) and immunosuppressant (IS) drug cocktail evaluation for the prevention or correction of cytokine storm and adaptive autoimmunity. The “High K_d ” cocktails were simulated with sub-optimal drug performance (Fig. S-10), while the “Lit. K_d ” cocktail was simulated with literature-value drug performance (Table S-IV). All three drugs in the antiviral cocktail were started at 6 dpi. For both immunosuppressant simulations, Dex treatment was started at 9 dpi and Toc treatment was started at 10 dpi. The simulations assumed severe disease, old age, male sex, and Delta variant.

TABLE I

Equations Corresponding to the Circuit

No.	Equation
(1)	$\frac{dV_{HC}}{dt} = -k_{inf}V_{HC} \left(\frac{V_{Vpop,f}}{K_{d,Vpop,f}} + \frac{V_{Vpop,i}}{K_{d,Vpop,i}} \right) - k_{HC,death,II} \left(\frac{V_{II,f}}{K_{d,II,HCd}} + \frac{V_{II,i}}{K_{d,II,HCd}} \right) - k_{HC,death,AAI} \left(\frac{V_{AAI}}{K_{d,AAI,HCd}} + \frac{V_{AAI,i}}{K_{d,AAI,HCd}} \right) + k_{HC,PopHom}(V_{HC,p} - V_{HC}) \frac{1}{1 + \left(\frac{V_{IC}}{K_{d,IC,PopHom}} \right)} + k_{IC,rec,VPM} \frac{V_{VPM,\tau} h_{VPM,\tau,ICrec}}{\left(\frac{V_{VPM,\tau}}{K_{d,VPM,\tau,ICrec}} \right) h_{VPM,\tau,ICrec} + \left(\frac{V_{VPM,\tau}}{K_{d,VPM,\tau,ICrec}} \right) h_{VPM,\tau,ICrec}}$
(2)	$\frac{dV_{IC}}{dt} = k_{inf}V_{HC} \left(\frac{V_{Vpop,f}}{K_{d,Vpop,f}} + \frac{V_{Vpop,i}}{K_{d,Vpop,i}} \right) - k_{IC,death,II} \left(\frac{V_{II,f}}{K_{d,II,ICd}} + \frac{V_{II,i}}{K_{d,II,ICd}} \right) - k_{IC,death,AAI} \left(\frac{V_{AAI}}{K_{d,AAI,ICd}} + \frac{V_{AAI,i}}{K_{d,AAI,ICd}} \right) - k_{IC,rec,VPM} \frac{V_{VPM}}{\left(\frac{V_{VPM}}{K_{d,VPM,ICd}} \right) + \left(\frac{V_{VPM}}{K_{d,VPM,ICd}} \right)} - k_{IC,rec,VPM} \frac{V_{VPM,\tau} h_{VPM,\tau,ICrec}}{\left(\frac{V_{VPM,\tau}}{K_{d,VPM,\tau,ICrec}} \right) h_{VPM,\tau,ICrec} + \left(\frac{V_{VPM,\tau}}{K_{d,VPM,\tau,ICrec}} \right) h_{VPM,\tau,ICrec}}$
(3)	$\frac{dV_{Vpop}}{dt} = \beta \frac{\left(\frac{V_{IC}}{K_{d,IC,bud}} + \frac{V_{Mol}}{K_{d,Mol}} + \left(\frac{V_{Pax}}{K_{d,Pax}} \right) + \left(\frac{V_{Pax}}{K_{d,Pax}} \right) \right) V_{Vpop}}{\tau_{Vpop} + \left(\frac{V_{II,f}}{K_{d,II,Vpop}} + \frac{V_{II,i}}{K_{d,II,Vpop}} \right) - \gamma_{II} \frac{\left(\frac{V_{II,f}}{K_{d,II,Vpop}} + \frac{V_{II,i}}{K_{d,II,Vpop}} \right)}{1 + \left(\frac{V_{II,f}}{K_{d,II,Vpop}} + \frac{V_{II,i}}{K_{d,II,Vpop}} \right)} - \gamma_{AI} \frac{\left(\frac{V_{AI}}{K_{d,AI,Vpop,kill}} + \frac{V_{AI}}{K_{d,AI,Vpop,kill}} \right)}{1 + \left(\frac{V_{AI}}{K_{d,AI,Vpop,kill}} + \frac{V_{AI}}{K_{d,AI,Vpop,kill}} \right)}$
(4)	$V_{Vpop,f} = V_{Vpop} \frac{1}{1 + \left(\frac{V_{AI}}{K_{d,AI,Vpop,bud}} + \left(\frac{V_{mAb}}{K_{d,mAb}} \right) \right)}$
(5)	$\frac{dV_{VPM}}{dt} = k_{VPM,pro} \frac{\left(\frac{V_{IC}}{K_{d,IC,VPM}} + \left(\frac{V_{Mol}}{K_{d,Mol}} + \left(\frac{V_{Pax}}{K_{d,Pax}} \right) + \left(\frac{V_{Pax}}{K_{d,Pax}} \right) \right) \right) V_{VPM}}{\tau_{VPM} + \left(\frac{V_{II,f}}{K_{d,II,VPM}} + \frac{V_{II,i}}{K_{d,II,VPM}} \right) - \gamma_{II} \frac{\left(\frac{V_{II,f}}{K_{d,II,VPM}} + \frac{V_{II,i}}{K_{d,II,VPM}} \right)}{1 + \left(\frac{V_{II,f}}{K_{d,II,VPM}} + \frac{V_{II,i}}{K_{d,II,VPM}} \right)} - \gamma_{AI} \frac{\left(\frac{V_{AI}}{K_{d,AI,VPM,kill}} + \frac{V_{AI}}{K_{d,AI,VPM,kill}} \right)}{1 + \left(\frac{V_{AI}}{K_{d,AI,VPM,kill}} + \frac{V_{AI}}{K_{d,AI,VPM,kill}} \right)}$
(6)	$\frac{dV_{VPM,\tau}}{dt} = k_{VPM,\tau} V_{VPM} - \frac{V_{VPM,\tau}}{\tau_{VPM,\tau}}$

Equation

$$\begin{aligned} \frac{dV_{II}}{dt} = & k_{II,act,IC} \left(\frac{V_{IC}}{K_{d,IC,IIact}} h_{IC,IIact} \right) + k_{II,act,Vpop} \left(\frac{V_{Vpop}}{K_{d,Vpop,IIact}} h_{Vpop,IIact} \right) + k_{II,act,VPM} \left(\frac{V_{VPM}}{K_{d,VPM,IIact}} h_{VPM,IIact} \right) + k_{II,pro,PF} \left[\left(\frac{V_{II,f}}{K_{d,II,PF}} \right) + \left(\frac{V_{Dex}}{K_{d,Dex}} \right) \right] + k_{II,pro,AI} \left[\left(\frac{V_{AI}}{K_{d,AI,IIpro}} \right) + \left(\frac{V_{Dex}}{K_{d,Dex}} \right) \right] \\ & + k_{II,CS,PF} \left[\frac{V_{II}}{1 + \left(\frac{V_{II,f}}{K_{d,II,CS,PF}} \right) h_{II,CS,PF}} + \left(\frac{V_{Dex}}{K_{d,Dex}} \right) \right] + \frac{V_{II}}{\tau_{II}} - k_{II,death} V_{II} \end{aligned}$$

$$V_{II,f} = V_{II} \frac{1}{1 + \left(\frac{V_{AAI}}{K_{d,AAI,II}} \right) + \left(\frac{V_{Toc}}{K_{d,Toc}} \right)}$$

$$\begin{aligned} \frac{dV_{AI}}{dt} = & \left(1 + \frac{V_{AI,mem}}{K_{AI,mem}} \right) k_{AI,act,ICTII} \left[\frac{V_{IC} V_{II}}{\left(1 - \frac{V_{AI,mem}}{\varphi_{AI,mem}} \right) K_{d,ICTII,AIact}} h_{ICTII,AIact} \right] + k_{AI,act,VpopII} \left[\frac{V_{Vpop} V_{II}}{\left(1 - \frac{V_{AI,mem}}{\varphi_{AI,mem}} \right) K_{d,VpopII,AIact}} h_{VpopII,AIact} \right] + k_{AI,act,VPMII} \left[\frac{V_{VPM} V_{II}}{\left(1 - \frac{V_{AI,mem}}{\varphi_{AI,mem}} \right) K_{d,VPMII,AIact}} h_{VPMII,AIact} \right] + \left(\frac{V_{Dex}}{K_{d,Dex}} \right) \\ & + k_{AI,pro,PF} \left[\left(\frac{V_{IC}}{K_{d,IC,AIproreg}} \right) + \left(\frac{V_{AI}}{K_{d,AI,PF}} \right) + \left(\frac{V_{Dex}}{K_{d,Dex}} \right) \right] + k_{AI,death} V_{AI} - \frac{V_{AI}}{\tau_{AI}} \end{aligned}$$

$$\frac{dV_{AI,mem}}{dt} = k_{AI,mem,pro,AI} \left(\frac{V_{AI}}{K_{d,AI,AI,mem}} \right) \frac{V_{AI,mem}}{1 + \left(\frac{V_{AI}}{K_{d,AI,AI,mem}} \right)} - \tau_{AI,mem}$$

Author Manuscript

Author Manuscript

Author Manuscript

Author Manuscript

Equation

$$\begin{aligned}
 \frac{dV_{AAI}}{dt} = & \left(1 + \frac{V_{AAI,mem}}{K_{AI,mem}} \right) \left[k_{AI,act,ICI} \left(\frac{V_{IC}V_{II}}{V_{AAI,mem} - \varphi_{AI,mem}} \right) \frac{h_{ICTI,AAI,act}}{1 + \left(\frac{V_{IC}V_{II}}{V_{AAI,mem} - \varphi_{AI,mem}} \right) \left(\frac{K_{d,ICTI,AAI,act}}{K_{d,AI,PF}} \right) + \left(\frac{V_{Dex}}{K_{d,Dex}} \right)} \right. \\
 & + k_{AI,act,ICII} \left(\frac{V_{IC}}{K_{d,IC,AI,prog}} \right) \frac{h_{ICII,AAI,act}}{1 + \left(\frac{V_{IC}}{K_{d,IC,AI,prog}} \right) \left(\frac{K_{d,ICII,AAI,act}}{K_{d,AI,PF}} \right) + \left(\frac{V_{Dex}}{K_{d,Dex}} \right)} \\
 & + k_{AI,act,VpopII} \left(\frac{V_{Vpop,J}}{K_{d,Vpop,AII}} \right) \frac{h_{VpopII,AAI,act}}{1 + \left(\frac{V_{Vpop,J}}{K_{d,Vpop,AII}} \right) \left(\frac{K_{d,VpopII,AAI,act}}{K_{d,AI,mem}} \right) + \left(\frac{V_{Dex}}{K_{d,Dex}} \right)} \\
 & + k_{AI,act,VPMII} \left(\frac{V_{V,PM,II}}{V_{AAI,mem} - \varphi_{AI,mem}} \right) \frac{h_{VPMII,AAI,act}}{1 + \left(\frac{V_{V,PM,II}}{V_{AAI,mem} - \varphi_{AI,mem}} \right) \left(\frac{K_{d,VPMII,AAI,act}}{K_{d,AI,mem}} \right) + \left(\frac{V_{Dex}}{K_{d,Dex}} \right)} \\
 & \left. + k_{AI,act,VPMII} \left(\frac{V_{V,PM,II}}{V_{AAI,mem} - \varphi_{AI,mem}} \right) \frac{h_{VPMII,AAI,act}}{1 + \left(\frac{V_{V,PM,II}}{V_{AAI,mem} - \varphi_{AI,mem}} \right) \left(\frac{K_{d,VPMII,AAI,act}}{K_{d,AI,mem}} \right) + \left(\frac{V_{Dex}}{K_{d,Dex}} \right)} \right]
 \end{aligned}$$

$$\frac{dV_{AAI,mem}}{dt} = k_{AI,mem,pro,AI} \frac{V_{AAI}}{K_{d,AI,AI,mem}} - \frac{V_{AAI,mem}}{\tau_{AI,mem}} \frac{V_{AAI}}{1 + \left(\frac{V_{AAI}}{K_{d,AI,AI,mem}} \right)}$$

Eq. 1

Eq. 2